Global Atmospheric OCS Trend Analysis from 22 NDACC Stations

James W Hannigan[1], Ivan Ortega[1], Shima Bahramvash Shams[2], Thomas Blumenstock[3], John Elliott Campbell[4], Stephanie Araz Conway[5], Victoria Flood[6], Omaira García[7], Michel Grutter[8], Frank Hase[9], Nicholas Brian Jones[10], Pascal Jeseck[11], Emmanuel Mahieu[12], Maria Makarova[13], Martine De Maziere[14], Isamu Morino[15], Isao Murata[16], Tomoo Nagahama[17], Hideaki Nakajima[15], Justus Notholt[18], Mathias Palm[19], Anatoliy Poberovskii[20], Markus Rettinger[21], John Robinson[22], Matthias Schneider[21], Amelie Röhling[21], Christian Servais[12], Dan Smale[23], Wolfgang Stremme[24], Kimberly Strong[5], Ralf Sussmann[25], Yao Té[26], Corinne Vigouroux[14], and Tyler Wizenberg[5]

[1]National Center for Atmospheric Research (UCAR)
[2]NCAR
[3]Karlsruhe Institute for Technology
[4]University of California, Merced
[5]University of Toronto
[6]Univ. Toronto
[7]Agencia Estatal de Meteorología (AEMET), CIAI
[8]Universidad Nacional Autónoma de México
[9]Institut fuer Meteorologie und
[10]University of Wollongong
[11]Sorbonne Université
[12]University of Liège
[13]Univ. of St. Petersburg
[14]Belgian Institute for Space Aeronomy
[15]National Institute for Environmental Studies
[16]Tohoku University
[17]Institute for Space-Earth Environmental Research, Nagoya University
[18]Institute of Environmental Physics, University of Bremen
[19]University of Bremen
[20]Univ of St. Petersburg
[21]Karlsruhe Institute of Technology
[22]NIWA
[23]NIWA Lauder
[24]UNAM, Mexico
[25]Karlsruhe Institute of Technology, IMK-IFU
[26]Laboratoire d'Etudes du Rayonnement et de la Matière en Astrophysique et Atmosphères (LERMA-IPSL)

November 24, 2022

Abstract

Carbonyl sulfide (OCS) is a non-hygroscopic trace species in the free troposphere and the primary sulfur reservoir maintained by direct oceanic, geologic, biogenic and anthropogenic emissions and the oxidation of other sulfur-containing source species. It's the largest source of sulfur transported to the stratosphere during volcanically quiescent periods. Data from 22 ground-based globally dispersed stations are used to derive trends in total and partial column OCS. Middle infrared spectral data are recorded by solar-viewing Fourier transform interferometers that are operated as part of the Network for the Detection of Atmospheric Composition Change between 1986 and 2020. Vertical information in the retrieved profiles provides analysis of discreet altitudinal regions. Trends are found to have well-defined inflection points. In two linear trend time periods ˜2002 - 2008 and ˜2008 - 2016, tropospheric trends range from ˜0.0 to (1.55 ± 0.30 %/y) in contrast to the prior period where all tropospheric trends are negative. Regression analyses show strongest correlation in the free troposphere with anthropogenic emissions. Stratospheric trends in the period ˜2008 - 2016 are positive up to (1.93 ± 0.26 %/y) except notably low latitude stations that have negative stratospheric trends. Since ˜2016, all stations show a free tropospheric decrease to 2020. Stratospheric OCS is regressed with simultaneously measured N$_2$O to derive a trend accounting for dynamical variability. Stratospheric lifetimes are derived and range from (54.1 ± 9.7)y in the sub-tropics to (103.4 ± 18.3)y in Antarctica. These unique long-term measurements provide new and critical constraints on the global OCS budget.

Global Atmospheric OCS Trend Analysis from 22 NDACC Stations

James W. Hannigan[1]

Ivan Ortega[1]

Shima Bahramvash Shams[1]

Thomas Blumenstock[2]

Elliott Campbell[17]

Stephanie Conway[3]

Victoria Flood[3]

Omaira Garcia[4]

Michel Grutter[5]

Frank Hase[2]

Pascal Jeseck[6]

Nicholas Jones[7]

Emmanuel Mahieu[8]

Maria Makarova[9]

Martine De Mazière[10]

Isamu Morino[11]

Isao Murata[12]

Toomo Nagahama[13]

Hideaki Nakijima[11]

Justus Notholt[14]

Mathias Palm[14]

Anatoliy Poberovskii[9]

Markus Rettinger[15]

John Robinson[16]

Amelie N. Röhling[2]

Matthias Schneider[2]

Christian Servais[8]

Dan Smale[16]

Wolfgang Stremme[5]

Kimberly Strong[3]

Ralf Sussmann[15]

Yao TE[6]

Corinne Vigouroux[10]

Tyler Wizenberg[3]

[1]National Center for Atmospheric Research, Boulder, CO, USA.
[2]Karlsruhe Institute of Technology (KIT), Institute of Meteorology and Climate Research (IMK-ASF), Karlsruhe, Germany
[3]Dept. of Physics, Univ. of Toronto, Toronto, ON, Canada
[4]Izaña Atmospheric Research Centre (IARC), State Meteorological Agency of Spain (AEMet), Santa Cruz de Tenerife, Spain.
[5]Centro de Ciencias de la Atmósfera, Universidad Nacional Autónoma de México, Mexico City, Mexico
[6]Laboratoire d'Etudes du Rayonnement et de la Matière en Astrophysique et Atmosphères, Sorbonne Université, CNRS, Observatoire de Paris, PSL Université, 75005 Paris, France
[7]School of Physics, University of Wollongong
[8]Institute of Astrophysics and Geophysics, University of Liège, Liège, Belgium
[9]Saint Petersburg State University, 79, Universitetskaya nab., Saint Petersburg, 199034, Russia
[10]Royal Belgian Institute for Space Aeronomy, Brussels, Belgium
[11]National Institute for Environmental Studies (NIES), Tsukuba, Ibaraki, 305-8506, Japan
[12]Graduate School of Environmental Studies, Tohoku University, Sendai, Miyagi, 980-8572, Japan
[13]Institute for Space-Earth Environmental Research (ISEE), Nagoya University, Nagoya 464-8601, Japan
[14]University of Bremen, Bremen, Germany
[15]Karlsruhe Institute of Technology, IMK-IFU, Garmisch-Partenkirchen, Germany
[16]National Institute for Water and Air, Lauder, Central Otego, New Zealand
[17]1156 High St, Santa Cruz, CA 95064

Key Points:

- Global distribution of OCS measured by NDACC solar absorption FTIR remote sensing,
- Tropospheric trends in OCS are non-monotonic globally, driven by anthropogenic emissions,
- Longest term stratospheric trends increasing outside of sub-tropics.

Corresponding author: James W. Hannigan, `jamesw@ucar.edu`

Abstract

Carbonyl sulfide (OCS) is a non-hygroscopic trace species in the free troposphere and the primary sulfur reservoir maintained by direct oceanic, geologic, biogenic and anthropogenic emissions and the oxidation of other sulfur-containing source species. It's the largest source of sulfur transported to the stratosphere during volcanically quiescent periods. Data from 22 ground-based globally dispersed stations are used to derive trends in total and partial column OCS. Middle infrared spectral data are recorded by solar-viewing Fourier transform interferometers that are operated as part of the Network for the Detection of Atmospheric Composition Change between 1986 and 2020. Vertical information in the retrieved profiles provides analysis of discreet altitudinal regions. Trends are found to have well-defined inflection points. In two linear trend time periods $\sim 2002-2008$ and $\sim 2008-2016$ tropospheric trends range from ˜0.0 to (1.55 ± 0.30 %/y) in contrast to the prior period where all tropospheric trends are negative. Regression analyses show strongest correlation in the free troposphere with anthropogenic emissions. Stratospheric trends in the period $\sim$ 2008 − 2016 are positive up to (1.93 ± 0.26 %/y) except notably low latitude stations that have negative stratospheric trends. Since $\sim$ 2016, all stations show a free tropospheric decrease to 2020. Stratospheric OCS is regressed with simultaneously measured N_2O to derive a trend accounting for dynamical variability. Stratospheric lifetimes are derived and range from (54.1 ± 9.7)y in the sub-tropics to (103.4 ± 18.3)y in Antarctica. These unique long-term measurements provide new and critical constraints on the global OCS budget.

Plain Language Summary

Carbonyl sulfide (OCS) is the most abundant sulfur containing gas in the atmosphere. There are many sources and sinks of OCS and other sulfur species in the atmosphere but all other sulfur species eventually are converted to OCS. It is important to quantify and understand OCS as it can be used to understand CO2 and the carbon cycle and also since it eventually is transported into the stratosphere where it maintains the sulphate aerosol layer at about 20km into the atmosphere. This layer is very important for earth's energy balance and climate change. In contrast with earlier and less comprehensive reports, this global study from 22 observation stations worldwide, shows stratospheric OCS to be increasing north and south of the equator but decreasing near the equator and to be increasing in the troposphere to 2016 and decreasing since. The main driver of OCS in troposphere are cumulative anthropogenic sources.

1 Introduction

Carbonyl sulfide (OCS) is the most abundant sulfur-containing compound in the atmosphere. The near-surface concentration is variable across much of the globe due to a diverse range of sources and sinks. It is chemically stable in the middle troposphere and a culminating reservoir for other abundant biogenic, anthropogenic and oceanic source species including di-methyl sulfide (DMS) and carbon disulfide (CS_2) see e.g. (Kettle et al., 2002; Ma et al., 2020). Consequently it is the largest persistent source of sulfur into the stratosphere (Sheng et al., 2015; Thomason & Peter, 2006) and a key contributor to the stability of the Junge sulfate aerosol layer in the lower stratosphere (Crutzen, 1976; Turco et al., 1980; Notholt et al., 2006; Kremser et al., 2016). Further OCS has both a direct and indirect effect on the earth's radiation budget as a maintainer of the aerosol layer and a direct absorber of middle infrared radiation (Crutzen, 1976; Turco et al., 1980).

The sources and sinks of OCS and OCS precursors are varied and complex (Zumkehr et al., 2018; Lee & Brimblecombe, 2016; Campbell et al., 2015; Suntharalingam et al., 2008; Kettle et al., 2002). The contribution of direct anthropogenic sources has been recently investigated (Zumkehr et al., 2018; Lee & Brimblecombe, 2016; Campbell et al., 2015). Both direct and indirect anthropogenic bottom up source inventories including rayon production, aluminum manufacture, coal burning, agriculture, pulp and paper manufacture, automobile tires and burning of biomass fuels (Zumkehr et al., 2018; Campbell et al., 2015) continue to be improved. Their emissions estimates are found to be non-monotonic in the time period studied (1980-2012), increasing in the most recent years, yet continues to maintain large uncertainties. Indirectly, biomass burning is an uncertain but not insignificant source of OCS (Stinecipher et al., 2019; Brühl et al., 2012; Notholt et al., 2003). The extent of biogenic uptake that has a large effect on annual cycles and possibly on long-term trends, especially in the Northern Hemisphere (NH) (Montzka et al., 2007), has also been elusive to define with certainty (Whelan et al., 2018; Wang et al., 2016; Suntharalingam et al., 2008).

OCS has become an important proxy measurement for understand CO_2 uptake by plants (Campbell et al., 2017). A thorough review of global OCS budget with focus on interactions with the biosphere has been undertaken by Whelan et al. (2018). There it is pointed out that to better enable the use of OCS on a large scale for CO_2 uptake or gross primary production (GPP) the proxy OCS budget needs to be improved, as the uncertainties in many sources and sinks limit its use. FTIR measurements of both OCS and CO_2 were employed in Wang et al. (2016) to observe seasonal cycles of both. Whelan et al. (2018); Wang et al. (2016) both conclude that top down budgets point to missing source(s). Furthermore, Hilton et al. (2017) in evaluating GPP related drawdown in North America using NOAA aircraft OCS measurements, differentiates plant fluxes from soil fluxes which the latter can approach 30% of the former.

The lifetime of tropospheric OCS is estimated at $2-3$y (Montzka et al., 2007). The persistent tropospheric concentration leads to a constant flux of OCS to the stratosphere (Crutzen, 1976; Turco et al., 1980; Kremser et al., 2015). There are no long-term direct sampling measurements of stratospheric OCS. OCS is a strong spectral absorber at 2030-2070 cm^{-1} in the mid infrared (MIR) and has been measured by remote sensing techniques from different platforms. Early latitudinal FTIR observations of stratospheric OCS from aircraft flying at 12km were made in 1978 by Mankin et al. (1979). In 2010, Coffey and Hannigan (2010) combined those with later aircraft measurements using the same instrument across a latitude range of $30°N-60°N$ and spanning 1978−2005 years to determine a positive but not significant trend of $(0.77 \pm 0.80)\%/y$.

A review of MIR spectral observations from ground-based, aircraft, balloon and Atmospheric Chemistry Experiment - Fourier Transform Spectrometer (ACE-FTS) satellite as well as new measurements from the Paris station and the Spectromètre Infrarouge d'Absorption à Lasers Embarqués (SPIRALE) balloon-borne instrument are described in Krysztofiak et al. (2015). With the wide range of latitude with these measurements they are able to show stronger seasonal amplitude of OCS in the total column and stratosphere with increasing latitude. The SPIRALE instrument also measured N_2O and they calculate stratospheric lifetimes of (68 ± 20) and (58 ± 14) years at 67°N and 5°S respectively. Due to the finite time span of the observations no trends are reported. More recently, Toon et al. (2018) used the 30 year (1989-2016) balloon-borne and ground-based MKIV FTIR dataset observed from various locations ranging from $34°N - 68°N$ and determine no significant trend in stratospheric OCS over that time period. This conclusion is similar to earlier reporting from aircraft measurements (Coffey & Hannigan, 2010) that spans a similar northern mid-latitude range.

Trends in OCS were deduced from the long-term ground based NDACC station at Kitt Peak ($32°N$) but not included in this work as the total column dataset ends in 2006. The initial work of Rinsland et al. (2002) is updated to the complete Kitt Peak observation record in Rinsland et al. (2008). The initial work focused on the middle tropospheric partial column excluding the tropopause region from 1978 to 2002 and showed a decreasing significant linear trend of $(-0.25\pm0.04)\%/y$, 1 sigma. Updated trends to 2005 and using updated spectroscopic line parameters reduced the downward trend to $(-0.1005\pm0.0028)\%/y$. Figure 4 of Rinsland et al. (2008) also reveal a sharp increase in number of observations after 1998 and a qualitative increase during that short time period between the two analyses $\sim 2002 - 2006$ that was not addressed at that time. Stratospheric observations from the 1985 ATMOS mission (ATMOS Spacelab3) (Zander et al., 1988), 1994 (ATLAS 3) (Gunson et al., 1996) and early ACE-FTS to 2008 (Barkley et al., 2008) measurements also showed no statistically significant increase in northern mid-latitude lower stratospheric OCS during that time (Rinsland et al., 2008) a similar finding as Toon et al. (2018) and Coffey and Hannigan (2010).

Most recently, ground-based measurements of OCS were analyzed for the Jungfraujoch station (Lejeune et al., 2016) and three stations in the southern hemisphere (Kremser et al., 2015) building on ground-based retrievals similar to Rinsland et al. (2002). Lejeune et al. (2016) specifically, explores and details the current retrieval for high resolution ground-based spectra. Both studies reveal generally upward trends in total and partial columns that have fairly well defined changes in trends. In particular Kremser et al. (2015) showed overall trends in total column OCS from 2001 to 2015 of $(0.73 \pm 0.03)\%/y$ at Wollongong, $(0.43\pm0.02)\%/y$ at Lauder, and $(0.45\pm0.05)\%/y$. at Arrival Heights. Although the time-series for each site showed a constant or decreasing burden between the years 2008 and 2012 depending on the station. A similar step in the trends was seen in the free tropospheric and stratospheric partial columns presented in that work. In Lejeune et al. (2016), they describe three distinct periods of stable trends for the total column at the northern mid-latitude Jungfraujoch station, decreasing during 1995-2002 by $(-0.62\pm 0.08)\%/y$, then increasing during 2002 - 2008 to $(1.21\pm0.10)\%/y$ and finally a lessening of the upward trend during 2008-2015 to $(0.23 \pm 0.10)\%/y$.

This work expands on the efforts of Kremser et al. (2015) and Lejeune et al. (2016) to characterize long-term trends of OCS in the lower and free troposphere and stratosphere globally. Datasets from 22 globally-dispersed sites have been combined to yield a composite view of OCS from 80°S to 80°N. Measurements have been made with NDACC standard instruments. Retrievals have been processed with all critical parameters predefined and employed by all research teams to provide a homogeneous final data product per NDACC standards. Trend analyses are performed by one group. The results are a single trend analysis of a harmonized global data series from a dispersed network of cooperating observation stations. Sec. 2 describes the stations and data collection and data processing. Sec. 3 describes the analysis of the time series, regression analyses, annual cycles, latitudinal distributions, stratospheric lifetimes and discussion from the global perspective. Sec 4. present the conclusions.

2 Stations and Observations

The data presented here leverage the organization of the NDACC *(www.ndacc.org)* (Kurylo & Soloman, 1990) to produce high-quality consistent long-term datasets from globally distributed stations. An overview of the NDACC can be found in De Mazière et al. (2018) published in Atmospheric Chemistry and Physics, in a joint special issue with Atmospheric Measurement Techniques and Earth System Science Data. Further information on the Infrared Working Group (IRWG) can be found at (`https://www2.acom.ucar.edu/irwg`) including lists of species data that are part of the standard IRWG data products. Data used for this analysis are available at *(www.ndacc.org)* and by request from the station PI.

2.1 Stations

There are 21 globally dispersed NDACC FTIR observation stations that comprise the IRWG, these are listed in Table 1. The station at CNRS, Paris (PAR) is not currently part of the IRWG though they make measurements in accordance with IRWG standards is included in the table. The map in Figure 1 shows the locations of the contributing stations. Observations from all sites continue to the present. Initial operations and consequent data record duration vary by station from Jungfraujoch in 1986 to Altzomoni in 2012.

Solar-viewing FTIR spectra are acquired in accordance with standards set forth by the IRWG *(www.acom.ucar.edu/irwg/links)*. These are high spectral resolution (minimum OPD=180cm, 250cm typical), instruments that can record spectra in selected spectral bandpass regions through the mid-infrared (MIR) from 750-5000 cm^{-1} and instruments that can record a single interferogram in under 1 minute. Observations are made routinely, often multiple times per day weather permitting. Several early ground-based OCS studies were performed (Mahieu et al., 1997) (Jungfraujoch), (Griffith et al., 1998) (Wollongong and Lauder) and (Rinsland et al., 2002, 2008) (Kitt Peak). More recently an analysis of southern hemisphere OCS was revisited by (Kremser et al., 2015) using data from the NDACC stations at Wollongong, Lauder and Arrival Heights. A thorough review of details and parameters to maximize information content and optimize profile retrieval from ground-based spectra was performed by Lejeune et al. (2016) using spectra from the Jungfraujoch.

2.2 Observations and Retrievals

The retrieval strategy adopted here is largely based on the optimized spectral regions and spectroscopy reported by Lejeune et al. (2016). Table 2 shows the micro-windows and species with absorption features that may affect the total spectral absorption. Three features of the ν_3 fundamental of OCS are fitted in the retrieval. The region at 2030 cm^{-1} is employed at some stations to improve the characterization of the interfering species of CO_2 and O_3. The spectroscopic parameters are based on HITRAN 2012 (Rothman et al., 2013). The ATM16 line parameter list (Geoff Toon, JPL, PC) was also tested to assess the linelist impact on OCS but for these OCS spectral regions did not result in an improvement in fit quality, interference from other species, or retrieved column.

The retrieval analysis for the ground-based FTIR spectra uses a form of the Optimal Estimation (OE) technique Rodgers (1976, 1990, 1998, 2000). There are two independent operational code sets that are used exclusively within the IRWG: these are PROFFIT (Hase, 2000) and SFIT (Pougatchev et al., 1995; Rinsland et al., 1998) (`https://wiki.ucar.edu/display/sfit4/`). They have been previously thoroughly inter-compared (Hase et al., 2004) and have been the algorithms used in many NDACC-wide trace gas trend analyses and validation efforts, e.g., (Gaudel et al., 2018; Olsen et al., 2017; Dammers et al., 2017; Buchholz et al., 2017; Vigouroux et al., 2015; Kohlhepp et al., 2012). The forward model and state vector rely on a priori data. Retrieval accuracy and precision are improved with a priori data as close to the observed state as possible (Pougatchev et al., 1995) and with statistically coherent associated uncertainties (covariances) (Rodgers, 2000).

Furthermore, for a globally distributed set of independent measurements as are employed here, internally consistent a priori data are needed. Much of this is incorporated in operational NDACC standards *(www.acom.ucar.edu/irwg/links)*. The retrieval grid is common for all sites at altitudes above ~ 7 km and adjusted consistently below ~ 7 km to accommodate the local observation altitude. Initial pressure and temperature profiles are NCEP analyses provided at *(www.ndacc.org)*, (Wild et al., 1995; Finger et al., 1993). For chemical a priori profiles of interfering species noted in Table 2, modeled climatological means are used.

Chemical profiles for all targeted NDACC and many background species have been generated from Whole-Atmosphere Community Climate Model, Version 4 (WACCM4) for all NDACC IRWG, NDACC LIDAR and many other stations for use as retrieval priors. These a priori profiles have several advantages over other sources of a priori information. The modeled data employs surface emission data that can provide more accurate low altitude mixing ratios that the FTIR retrieval may not be sensitive to and may not be included in other a priori sources eg satellite profiles. The derived mean a priori from a long-term model run also yields a measure of variability that can be used as the covariance for retrievals and for understanding smoothing by the retrieval. To the accuracy of the model, the interspecies correlations are self-consistent. The global surface to mesosphere model provides consistency for all sites in the altitude range of interest, and sensitivity of the FTIR retrievals. There is no observational dataset with this complete self-consistency for more then 60 trace species otherwise available for this purpose, consequently, the IRWG adopted a run of the WACCM4 model (Garcia et al., 2007) for priors for retrieved species and for profiles for background or interfering species. To provide a priori that are minimally biased over the long-term, the a priori are computed as an average from monthly sampling of the 40 year portion from 1980-2020 of a 75 year Stratosphere-troposphere Processes And their Role in Climate (SPARC) Chemistry Climate Model Initiative (CCMI) model inter-comparison. The CCMI validation was a continuation of the CCMVal project as described in Eyring et al. (2007) and compares several models under specific Intergovernmental Panel on Climate Change (IPCC) scenarios for O_3 recovery. In particular we use a moderate set of scenarios following REFC1.3 and IPCC scenarios A1B for greenhouse gases emissions, AR4 for sea surface temperatures and surface Halogen Ab prescribed by WMO/UNEP. Details can be found in Eyring et al. (2007). These a priori chemical profiles, interpolated to station location and altitude, provide a reasonable mean from which observations will vary. The a priori profiles were tested for applicability at all sites before adoption as an NDACC a priori standard.

Unfortunately profiles for OCS are not included in the large suite of WACCM4 species (we expect these will be part of the forthcoming version). In order to attain a globally consistent a priori dataset that also spans the net OCS seasonal cycle, datasets from the National Science Foundation (NSF) High-performance Instrumented Airborne Platform for Environmental Research (HIAPER) airborne campaign Pole-to-Pole Observations (HIPPO) (`www.eol.ucar.edu/field\_projects/hippo`) and satellite-borne ACE-FTS (`www.ace.uwaterloo.ca/instruments\_acefts.php`) (Boone et al., 2013) were used. The tropospheric dataset, used for the profile component below 14 km, is comprised of the accumulated datasets from HIPPO missions 1 through 5, spanning a latitude range of 85°N to 67°S reaching all FTIR stations but Arrival Heights sampling different seasons over a 2.4 year operational window during 2009-2011 (Wofsy, 2011; Wofsy et al., 2017). The stratospheric portion of OCS is obtained from ACE-FTS v3.5 between 2004-2013 (Boone et al., 2013; Velazco et al., 2011). From these data, mean profiles and covariances were derived. To account for latitudinal variability without over-burdening the somewhat sparse HIPPO dataset composite profiles were binned into five zonal regimes: $90-50°N$, $50-20°N$, $20°N-20°S$, $20-50°S$, and $50-90°S$. Table 3 lists the number of raw profiles available for reduction to zonal a priori. The profiles were interpolated to a 1 km grid, averaged for each latitude bin and concatenated at 14 km. The ACE-FTS derived zonal profiles were found to be biased low by $\sim 15\%$ relative to the HIPPO datasets at 14 km. A similar negative bias for the ACE-FTS OCS has also been reported previously with respect to the MK-IV FTS (Velazco et al., 2011), MIPAS (Glatthor et al., 2017) and SPIRALE (Krysztofiak et al., 2015). Consequently for purposes here, a positive shift of $\sim 15\%$ is applied to the ACE-FTS profiles to match the upper tropospheric portion of the HIPPO in situ profiles. Above the ACE-FTS max altitude, the profiles were tapered to 0.015 pptv (parts per trillion by volume) at 50km and above with no consequence to this analysis, due to the rapidly diminishing sensitivity above $30km$ altitude. The profiles were smoothed by a Savitsky-Golay function with a 9km window width and polynomial of order 3. The left panel of Figure 2 show the final concatenated and smoothed a priori vertical profiles binned to latitudinal zones. The right panel Figure 2 are 1 σ (σ will be used consistently to note 1 standard deviation of the population being discussed) curves derived from all contributing profiles. These curves are then used as initial diagonal components of the a priori state vector covariances (S_a) in the OE retrieval scheme. To create the OCS retrieval S_a matrix the diagonal elements are interpolated and normalized to the variable layer thickness retrieval grid by the square root of the thickness. Finally the off-diagonal elements of the S_a matrix are calculated using a Gaussian function with a 4km halfwidth that aids in maximizing information content.

The profile retrievals are shown in Figure 3. This figure (and several similar to follow) show results for each station with panels displayed from high to low latitude, top to bottom of the figure. The background color shading illustrates the five latitude zones given in Table 3. The vertical response of the retrieval is characterized in the averaging kernels (AK) and by the accumulated scalar degrees of freedom for signal (DOFS) (Rodgers, 1998, 2000). These are shown for all sites in Figure 4. For each site, the left panel are the common retrieval grid volume mixing ratio (VMR) averaging kernels. These show the typical broad kernels that are indicative of the limited vertical resolution of the retrieval system. Yet, they also reveal peaks in the troposphere and lower stratosphere that we exploit in the multi-layer analysis. The middle panels are the total column averaging kernel indicating the altitude sensitivity of the integrated total column amount. The right panels are the accumulated DOFS summed from the observation altitude upwards, where DOFS values vary over a small range from ~ 2.5 at lower latitudes to ~ 3 at higher latitudes but will also depend on station altitude and the instrument signal-to-noise (SNR).

2.2.1 Uncertainties and Information Content

An uncertainty analysis for the state vector for all species retrieved within the guidance of the NDACC IRWG follow the formalism of the OE technique (Rodgers, 1990). The uncertainty calculations are part of the standard IRWG retrieval processing to maintain homogeneity across the network and species and is discussed in a number of publications, e.g. (Vigouroux et al., 2008; Lejeune et al., 2016; Vigouroux et al., 2018). This reveals the quantitative contribution of the principle components of the observation and retrieval system to the uncertainty in the state vector and in particular the retrieved VMR profiles. Given the homogeneity of the observing systems from instrumentation through retrieval, we detail here, representative uncertainty budgets for three stations: TAB, BLD and MLO. They represent a range of observation characteristics that can effect a ground-based retrieval and its associated uncertainty. These stations span a range of latitudes: $20, 40, 76°N$, of observation altitudes: .22, 1.6, 3.45 km.a.s.l., proximity to anthropogenic or biogenic sources from remote Arctic to continental suburban mid-latitude to sub-tropic Pacific island. Uncertainty profiles for principle uncertainty components are calculated at each altitude layer for each retrieval. Uncertainty profiles for random and systematic components for a single retrieval from each site are plotted in Figure 5 in percent of the a priori VMR profile.

Random components are the measurement, interfering species, temperature profile variability, solar zenith angle and background retrieval parameters. Of these all remain below 2% of the VMR profile for all altitudes except the measurement error which peaks in the stratosphere between 25 and 28km and varies in magnitude with station at 15%, 10% and 6% at TAB, BLD and MLO respectively. Systematic components are the temperature profile bias, phase function, HITRAN parameters: line intensity (S), air broadened half width (γ) and the coefficient of the temperature dependence of the air-broadened half width (n). Of these all contribute less than 3% except the air broadened half width which contributes up to 12% at 13km at TAB, between 7.5 and 9.5% between 12 and 26km at BLD and peaking at 26km at 13% at MLO.

More appropriate for the data presented below, are the random, systematic and total uncertainties expected for each analysis layer (LT, FT, LS) for these three sites. Table 4 gives the mean and standard deviation uncertainties for a single retrieval in pptv from the average of retrievals in 2019. The low standard deviations illustrate the consistency of the typical data discussed here. The rightmost column are the accumulated DOFS in that layer for that site and as noted can vary with station latitude and observation altitude. The total DOFS increase from 2.0 to 3.3 with increasing latitutude as do the stratospheric partial columns from 0.9 at MLO to 1.9 at TAB. The free tropospheric DOFS primarily reflect the tropopause height and decrease with latitude with a minimum of 0.6 at TAB. This is slightly lower than the low troposphere at TAB of 0.7. We expect all stations to follow similar patterns and quantitatively similar DOFS. The lowest value is seen at BLD with an observation altitude of 1.6km and a free tropospheric upper limit at 4km. Other stations that would also have low tropospheric DOFS are Maïdo at 2160 m.a.s.l. and Izãna at 2370 m.a.s.l.. Stations nearer sea level will typically have larger overall DOFS. Although these few stations with low DOFS have lower information we keep the data series to complete the analysis and note the data may include more information from the a priori than the others.

Regarding layer independence, from Figure 3 it can be seen that retrievals exhibit slightly lower mixing ratios than the a priori for the tropospheric layers and not seen systematically in stratospheric retrievals. The actual biases are given in Table 5. Biases range from -0.80 pptv at TSK to -11.92 at PAR in the LT and -1.049 at BRE to -10.21 at PMB in the FT. Although the differences at MAI of -2.9 and -3.1 are small, at IZA the LT bias is -8.4 pptv whereas the FT bias is -4.27.

3 Time Series and Long-Term Trends

The time series data will be represented with monthly means of the total column and partial columns that are given as mean mixing ratios for altitude regimes commensurate with the DOFS of the retrievals and detailed below.

Figure 6 shows the time series of monthly mean total columns for all stations. The monthly means retain the long-term trend information excluding very short-term variability. Column or concentration data for each site is plotted using the same ordinate and abscissa scale to more easily illustrate the global perspective on trends at all sites. Variation in station altitude and latitude are reflected in the total column amounts. All sites show an annual cycle that is affected in part by the annual variation of the aggregate of sources and sinks and tropopause height (latitude dependent). The large step in the data for the St Denis - Maïdo (STD-MAI) station which is the concatenation of the St Denis station data record (early) and Maïdo record (later data) is due to the altitude change from the St Denis site at sea level to Maïdo at 2.16 km.a.s.l.

To analyze the long-term trend and annual cycle and account for unevenly sampled time series when needed, we use a bootstrap re-sampling tool (Gardiner et al., 2008) and Eqn. 1:

$$f(t) = a_0 + a_1 (t - t_0) + \sum_{n=1}^{N} b_n \cos\left(\frac{n\pi x}{L}\right) + \sum_{n=1}^{N} c_n \sin\left(\frac{n\pi x}{L}\right) \tag{1}$$

where the first two terms correspond to the linear component: a_0 is the intercept value, a_1 is the long-term trend (or slope) of the observation time t, and t_0 is the time of the first observation. The second and third terms are the Fourier series to fit the seasonal modulation where $N = 2$. A bootstrap population of 5000 is used, yielding the mean slope (a_1) and distribution halfwidth that are used to quantify the trend and its 1σ uncertainty. The annual rate of change relative to the mean, calculated with the linear portion of Eqn. 1, is estimated with the anomalies ($FTIR(t) - f(t)$) using the seasonal components of the fit calculated with Eqn. 1 to account for seasonal variability.

Figure 7 shows the total column anomalies now fitted with a 5^{th} order polynomial to illustrate slowly varying changes in the trend (blue line). The total column data is generally increasing at all these stations over this time period but not monotonically. The polynomial fit reveals changes from a linear trend. For the longest term sites, these show a minimum in 2001-2002. For most of these another change in slope is at ~ 2008. Similar inflection points were exhibited in earlier work in the southern (Kremser et al., 2015), and northern (Lejeune et al., 2016) hemispheres and here are shown to be a more universal feature seen in the dataset globally. We will discuss trends in these time periods below. As mentioned in the Introduction total column from Kitt Peak show a decreasing linear trend from $1978 - 2002$ of $(-0.25 \pm 0.04\%/y)$ (Rinsland et al., 2002) and of $(-0.1005 \pm 0.0028\%/y)$ shown in Figure 4 in Rinsland et al. (2008). The later also shows a qualitative leveling during that short time period between $2002 - 2006$ that while not addressed at that time is a feature seen at other stations (see below).

The longer Arctic time series (NYA, TAB, KIR) seem to show a delay in this feature. There is a slow increase to 2006 then a leveling off or decline with a resumed increase nearer 2014. In TAB this is offset by anomalously high values in early 2016. In the SH high values are seen at two stations WLG and AHS in $1996 - 1999$ before rapidly dropping to minima around 2002.

We have obtained data for most stations up through 2019 or 2020. Figure 7 clearly show another likely inflection point other than those described above, in the time series record at the period $\sim (2016 - 2018)$ at stations e.g. TAB, KIR, TOR, LDR and AHS. To draw conclusions on the increasing trends in the last decade we calculate a linear trend for the $2008 - 2016$ period as discussed below. The inflection point at $\sim (2016 - 2018)$ seen in Figure 7 is clear but too recent and too short a time period to draw any conclusion as to the current rate of the decrease.

3.1 Tropopause Height and Layer Isolation

The latitudinally dependent annual cycle of the tropopause height (TH) coupled with the OCS vertical profile (see Figure 3) that rapidly decreases above the tropopause imposes a problematic annual signal on the retrieved profiles. To make the best use of the limited vertical resolution illustrated in Figure 4, while minimizing the effect of the variable TH, layers relative to the tropopause are defined. Further the mean mixing ratio, that is independent of the optical path through the the layer is calculated. Table 6 shows the NCEP temperature derived tropopause height for each station. We compared this TH method with the more precise dynamical tropopause height (Zängl & Hoinka, 2001) (and M. von Hobe, PC) and found this method adequate for this analysis due to the coarse vertical resolution of the measurements.

Altitude ranges are chosen in an attempt to isolate the free troposphere where OCS dominates the sulfur budget, from large surface sources and sinks regime and stratosphere while minimizing the effects of annual tropopause height cycles which vary in altitude with latitude to clarify long-term trends distinguishing the source region from the stratosphere. As shown in Figure 4 the OCS retrievals yield sufficient information (DOFS up to ~ 3) to detail three altitude ranges. These analysis ranges are: observation altitude to 4 km, 4 km to TH - 2σ and TH + 2σ to 40 km. The choice of 4 km also keeps the free tropospheric region from high altitude sites e.g. JFJ, MLO, ALT on equal footing as other sites see Table 1.

3.2 Trends by layer

On the standardized retrieval grid there is still a small variation in layer thickness nearer the observation altitude for each site. We define a weighted mixing ratio (wVMR) for the three integrated analysis layers calculated with the following expression:

$$wVMR = \frac{\sum_{z=1}^{n} x_z \cdot K_z}{\sum_{z=1}^{n} K_z} \tag{2}$$

where $wVMR$ is the final weighted mixing ratio of OCS in that layer, z is the altitude layer on the retrieval grid, x_z is the retrieved mixing ratio in that layer, and K_z is the associated air mass. The $wVMR$ is an easily comparable quantity independent of the actual layer thickness which varies at each latitude.

Figure 8 shows the anomalies for the lower tropospheric (LT) layer monthly mean mixing ratios, segregated into periods of general linear trend. Observation altitude for stations ALZ, JFJ, MLO are above this layer. Due to the complex sources and sinks we might expect more variability from station to station in this altitude regime. The high northern latitude stations have a range of increasing rates in the last decade (2008-2016) from EUR (0.08 $\pm$ 0.17 %/y) to NYA (0.30 $\pm$ 0.14 %/y). TAB has a recent rate of (1.55 $\pm$ 0.30 %/y) but is biased due to very high values in spring 2016 attributed to an anomalous local natural event. At and below the Arctic circle KIR clearly shows a minima in 2002 and an increase of (0.19 $\pm$ 0.08 %/y), the fore shortened series at STP shows a strong increase of (0.96 $\pm$ 0.14 %/y) and no trend at BRE (0.07 $\pm$ 0.07 %/y). Some northern mid-latitude stations show more to excessive variability e.g. (PAR, TSK, RKB) which may be due anthropogenic sources though notably quiescent in the northern mid-latitudes is BLD which would have less oceanic and possibly less anthropogenic influence. All northern mid-latitude stations show positive trends 2008 - 2016 of (0.11 - 1.03 %/y) except BLD at (0.02 $\pm$ 0.10 %/y) and RKB due to a period of no data. In the subtropics PMB has a positive trend with (0.31 $\pm$ 0.13 %/y).

The composite record from St. Denis and Maïdo stations have a strong positive tropospheric trend of (1.01 $\pm$ 0.09 %/y) at higher southern latitudes. Anomalous inflections are clear in longer term records in the SH e.g. LDR, WLG, AHS as are trends, as seen in Kremser et al. (2015). These increase moving south at (0.19 $\pm$ 0.04 %/y), (0.24 $\pm$ 0.08 %/y) and (0.68 $\pm$ 0.12 %/y) at WLG, LDR and AHS.

Figure 9 is similarly formatted as Figure 8 but for the free tropospheric (FT) monthly mean mixing ratios. The six high northern latitude station records all show a positive increase in the past decade. These range from (0.06 $\pm$ 0.05 %/y) at BRE to (0.87 $\pm$ 0.16 %/y) at TAB. Excluding TAB, the range is from 0.06 to (0.45 $\pm$ 0.12 %/y) at NYA. The high trend at TAB is primarily due to the high values seen in spring 2016. The longer term records in the Arctic have positive trends of (0.52 $\pm$ 0.06 %/y) at TAB (1999) and (0.38 $\pm$ 0.03 %/y) at KIR (1996). Of the northern mid-latitude stations PAR and BLD, their records show shallow non-significant trends while the others are all positive and range from (0.25 $\pm$ 0.04 %/y) at IZA to (0.76 $\pm$ 0.11 %/y) observed at TOR. Two long-term northern mid-latitude data records clearly show the minimum in 2002: ZUG (began 1995) and JFJ (began 1986). Prior to that, during the period 1996−2002, their trends were strongly negative at (-1.09 ± 0.12 %/y) and (-0.66 ± 0.04 %/y) respectively. The JFJ station has the longest data series, and although variability is larger in the earliest years, the downward, nearly linear trend clearly persisted since at least the inception of the record. The linear trend of the complete record for these two sites in the free troposphere are (0.34 ± 0.03 %/y) and (0.05 ± 0.02 %/y) respectively.

The subtropical stations have two at high altitude at ALZ and MLO. The ALZ time series begins in 2012 and has positive trend at (0.32 ± 0.13 %/y), while both PMB and MLO show stronger trends at (0.48 ± 0.14 %/y) and (0.60 ± 0.08 %/y) respectively, although both, especially PMB, contain periods of sparse data in the observational record. The MLO station data series begins in 1995, the linear trend from that time is (0.31 ± 0.02%/y). Of the four southern hemisphere stations STD-MAI shows a non-significant trend at (-0.02 ± 0.06 %/y), the others are positive in the past decade with (0.23 ± 0.02 %/y), (0.38 ± 0.03 %/y) and (0.45 ± 0.05 %/y) for WLG, LDR and AHS respectively. The two stations with the longest term records, at WLG (began 1996) and AHS (began 1997) have linear trends in the free troposphere of (0.28 ± 0.02 %/y) and (0.32 ± 0.02 %/y) respectively.

Although observations clearly show consistent trend fluctuations over the 36y (for JFJ and 26y for most other stations) FTIR record, globally, the free tropospheric OCS mixing ratio has increased between 0.05 (since 1986) or 0.28 (since mid 1990's) and 0.52 %/y. As noted above with regard to the total column time series, the very recent fall off since 2016 - 2017 is seen in several sites e.g. ZUG, IZA, in the lower tropospheric time series. This is more clear and widespread in the free tropospheric data e.g. TAB, KIR, JFJ, STD-MAI, LDR, AHS.

Figure 10 is similarly formatted as Figure 8 but for the stratospheric (ST) monthly mean mixing ratios. For the three high arctic sites, two show positive trends for the past decade of (0.33 ± 0.27 %/y), (0.23 ± 0.24 %/y) for EUR, NYA but at TAB there is non-significant negative trend of (-0.28 ± 0.29 %/y). For the prior period 2002-2008 both NYA and TAB are strongly increasing by (1.13 ± 0.38 %/y) and (1.33 ± 0.58 %/y) respectively. The three next highest latitude sites show increases of (0.71 ± 0.30 %/y), (1.61 ± 0.30 %/y), (0.81 ± 0.39 %/y) at KIR, STP and BRE respectively. Furthermore of the high northern mid-latitude sites that have longer term records TAB (1999) has a non-significant overall trend of (0.06 ± 0.12 %/y), and KIR (1996) at (0.26 ± 0.10 %/y). In the northern mid-latitudes, all eight stations show a positive increase in the 2008-2016 period ranging from (0.30 ± 0.23 %/y) at JFJ to (1.56 ± 0.52 %/y) at PAR, with PAR, BLD and IZA all greater than 1%/y. In the subtropics both MLO and ALZ show comparable negative rates of change at (-0.48 ± 0.20 %/y), (-0.54 ± 0.37 %/y) respectively while the sparse PMB at 5.8°N shows an increase of (0.29 ± 0.16 %/y). Similarly all southern hemisphere stations show an increase of (1.93 ± 0.26 %/y), (1.01 ± 0.28 %/y), (1.12 ± 0.17 %/y), (0.31 ± 0.58 %/y) at STD-MAI, WLG, LDR and AHS respectively.

The longest term linear trends of the stratosphere are slightly more varied. In central Europe the trend at JFJ since 1986 is (0.23 ± 0.04 %/y) while nearby at ZUG since 1995 it is higher at (0.35 ± 0.06 %/y). At high northern latitudes at KIR the positive trend is (0.26 ± 0.10 %/y) while higher at 70°N the trend at TAB is non-significant at (0.06 ± 0.12 %/y). In the subtropics, MLO shows a slight negative trend since 1995 at (-0.08 ± 0.04 %/y). In the southern hemisphere WLG has a non-significant trend of (0.04 ± 0.08 %/y) while at AHS at 79°S the trend since 1997 is (0.47 ± 0.15 %/y).

Generally the stratospheric mean monthly mixing ratios have more variability than the tropospheric values due in part to the increased uncertainty with this component of the retrieved profile. Nevertheless, of significance is the absence of the partial column fall off since $\sim$ 2017 seen in both the lower and largely in the free tropospheric partial column time series at most sites. Given the tropospheric lifetime for OCS of $\sim 2-3$y (Montzka et al., 2007), if the tropospheric trend continues it may be realized in the stratosphere in the near future.

3.2.1 Summary of Segmented Trends

A summary of the linear trends for the three atmospheric layers within three time periods since 1996 and for the several longest time series since inception is given in Figure 11. Panel a shows the trends for the longest term stations from their inception until 2016 for lower troposphere (red), free troposphere (blue) and stratosphere (green). Panel b are the linear trends until 2002 for stations that begin at latest in 1996 (1999 TAB). Panel c similar as panel b until 2008 for stations starting at latest in 2002 and panel d are the latest trends from 2008 to 2016. From panel b: of the 8 years leading to

2002 all tropospheric trends are strongly decreasing from (-0.39 ± 0.13 %/y) at WLG in the free troposphere to (-1.29 ± 0.20 %/y) KIR in the lower troposphere. During this time stations in the southern hemisphere have non-significant positive trends as does KIR at 67°N. MLO has a positive trend with high variability of (0.27 ± 0.25 %/y). The remaining data records in in northern mid-latitudes with positive stratospheric trends at ZUG (0.69 ± 0.38 %/y), at JFJ (0.40 ± 0.12 %/y) and at RKB (0.61 ± 0.37 %/y).

3.3 Free tropospheric Trends and Proxy Regression

The basis for the segmented linear regions are the consistent inflection points for the longest term data series illustrated in Figure 7 and seen more clearly in the FT anomaly data series in Figure 9. To attempt to define drivers of this multi-year variability, a two-part regression approach is applied to the FT anomaly time series isolating proxies by zonal bands given in Table 3. The first step uses a Stepwise Multiple Regression (SMR) (Appenzeller et al., 2000; Brunner et al., 2006; Kivi et al., 2007; Vigouroux et al., 2015; Bahramvash Shams et al., 2019) where the contribution of proxies are investigated for each site to determine a dominant set for the stations to be used in the second regression run for all sites in that zone (Wohltmann et al., 2007; Bahramvash Shams et al., 2019). This method avoids spurious correlation of proxies and OCS (Wohltmann et al., 2007). Forward selection criteria are the highest explained variance (R^2) and p-value lower than 0.05 of the SMR (Sect. 7.4.2, Wilks (2011)). The iteration converges when no variable can increase the R^2 by more than 1%. The description and source for each proxy is given in Table 7

To conserve the local variability of SST, eleven SST regional averages are estimated for use in the SMR. Zonally averaged Normalized Difference Vegetation Index (NDVI) and Chlorophyll index (CHLOR) use latitude ranges as in Figure 3. Multivariate ENSO Index (MEI), time lag of 0 to 4 months are used (Randel et al., 2009; Vigouroux et al., 2015; Bahramvash Shams et al., 2019). However, the selection process will remove all but at most one. The resulting correlation coefficients among variables are less than 40% except for regional MEI with tropical SST (20S-20N) and where only SST is used in the final model. This regression is applied to a subset of data and proxies that overlap in the time period 2004 - 2017 and due to the short MAI time series, it is excluded. Selected mutual proxies are similar for LT and FT so the final regression is given for the FT anomalies. SST is a mutually selected proxy in all regions. NDVI is found to be dominant in the sub-tropics and all northern zonal bins, MEI in the north mid-latitude ($20° - 50°N$) only and sea ice extent in the Arctic ($50° - 90°N$) only.

Due to long lifetime of OCS, we expect a high degree of autoregressive structure in OCS time series. The Cochrane-Orcutt correction (COC) is applied in the final model (Cochrane & Orcutt, 1949). The results of the final regression are shown in Figure 12. They emphasize the accumulation of OCS seen in the improvement of R^2 with application of the COC. Using COC the selected variables are able to explain the fluctuations of the anomalies FT OCS time series by R^2 more than 78% in 16 of 21 stations as shown in the upper left of each station panel in Figure 12.

Excluding the COC the geophysical and biogenic proxies account for at most 32% of variability. A recently revised anthropogenic emissions inventory is shown in Figure 2 of Zumkehr et al. (2018) but is currently available only for 1980 - 2012 on an annual basis. Using JFJ time series with the record of closest overlap of 1986 - 2012, a simple annual regression with no auto-correlation correction yields a high value of $R^2 = 70\%$. The Zumkehr et al. (2018) record ends in 2012, though the observational records here show a clear continued increase to $\sim 2016-2017$ followed by a period of rapid decline to 2020. Given the correlations biogenic, oceanic and anthropogenic proxies above, there is a high degree of confidence the FT OCS concentrations are strongly influenced by anthropogenic sources since at least the mid 1980's.

3.4 Stratospheric Trends using a Dynamical Proxy Regression

Stratospheric N_2O has been shown to be effective as a proxy to attempt to account for stratospheric dynamical effects that would effect all long lived trace species and so diminish the variations in the trend of a stratospheric species (Rinsland et al., 2008; Stolarski et al., 2018; Toon et al., 2018). N_2O is a standard retrieval species within the NDACC IRWG and available at the NDACC Data Handling Facility (DHF) for all stations (Zhou et al., 2019). N_2O time series are retrieved in a standardized manner using the same forward model and on the same retrieval grid as the OCS (see *www.acom.ucar.edu/irwg/links)* across the network to form a globally harmonized data product. For this work the retrieved N_2O profiles were processed identically as the OCS to produce a co-located monthly mean stratospheric N_2O wVMR time series. The stratospheric N_2O time series given by P_{N_2O} in Equation 3 is used as a regression proxy for the longest term stations. Since N_2O

has been increasing at $\sim 0.25\%/y$, (Stolarski et al., 2018), P_{N_2O} is decreased at this rate rendering m_1 the linear trend of OCS after fitting.

$$f_{N_2O}(x) = a_0 + a_1 x + b_0 P_{N_2O}(x) x = t - t_0 \quad (3)$$

To allow a direct global comparison from the stations with the longest data records still representing a wide range of latitudes, the trends given here are the same duration of 2001 - 2016 for all stations. The results of this process on the regression and trends are shown in Figure 13. Generally the process improves the R-values compared in Figure 13 panel a, for most stations except for MLO and LDR. Panel b shows only slight changes in residuals that are all improved except for LDR. Panel c compares the trends with the straight long-term linear regression where most trends increase though within uncertainties, which includes MLO that becomes less negative. WLG becomes much more negative and LDR slightly more though both still within uncertainties.

Based on these long-term regressions northern mid-latitude to Arctic stratospheric trends are increasing from (0.12 ± 0.09 %/y) (0.32 ± 0.12 %/y) (0.25 ± 0.07 %/y) (0.28 ± 0.09 %/y) (0.28 ± 0.11 %/y) at TAB, KIR, ZUG, JFJ and IZA respectively. At 19.5°N and −34.4°S the stratospheric trends are negative at (-0.10 ± 0.07 %/y) and (-0.24 ± 0.12 %/y) at MLO and WLG respectively. LDR has similar positive rate to northern mid-latitudes at (0.27 ± 0.06 %/y) and the largest increase is seen at AHS of (0.79 ± 0.19 %/y). This represents a strong accumulation of stratospheric OCS in the Antarctic in recent years that appears to not be represented in the analysis of Kremser et al. (2016) in which trends ended in 2016.

3.5 Annual Cycles

Monthly seasonal variations of wVMR with $\pm 1\sigma$ of the average are presented in Figure 14. The FTIR monthly means are color coded by site (see legends) and presented for the three layers and latitude bins. Tropospheric cycles at Arctic stations show a large annual change from highs near 500 pptv in late spring at EUR, NYA and TAB to lows below 370 pptv in lates summer. Recently de-iced oceanic sources may account for excess spring amounts (Becagli et al., 2016). Of note is the larger year to year range seen at STP as opposed to BRE pointing to more varied local sources or sinks. More stable are the FT cycles but still with the largest changes at higher latitudes. In the stratosphere all high latitude sites peak in September or October with maxima between 280 and 340 pptv increasing poleward.

At northern mid-latitudes in the LT the peak in the cycle for several sites TSK, RKB is April, for most sites it is May but for PAR it is May-June and Jun-Jul for BLD. TSK, while it exhibits the largest variability also has a secondary peak in October. While PAR has a large drop from 460 pptv in July to 425 in August. In the FT aside from TSK which maintains high values from April to September and BLD which peaks in July all sites peak in June. Northern mid-latitude stratospheric values show the larges range in OCS mixing ratios with longitude with BLD maintaining the highest values of up to 360 pptv in summer and fall months. The BLD time series is short, recently starting in 2010 which may tend to bias towards higher averaged wVMR's. Annual variations are on the order of 50 pptv.

The three tropical sites do not well characterize the longitudinal space (see Table 1). Both the LT and FT have a maximum in May. PAR have a minimum in November while ALZ and MLO have minima in October. MLO tends to maintain low values through to February while ALZ rebounds and PAR appears to in December but has limited observations due to seasonal cloud cover. LS values above 300 pptv are maintained throughout the year as there is a small seasonal cycle amplitude of 20 pptv. ALZ and MLO tend to see highest values in September while PAR has highest monthly means in February.

Similarly the three lower mid-latitude sites do not well characterize the longitudinal space. In the LT STD-MAI in the Indian Ocean sees little seasonal variation but fairly high sustained values year round between 460-480 pptv. Both LDR and WLG further East and South and on much larger land masses show clear similar cycles with peaks in January - February and minimums in early winter in June. LDR shows a concentration about 30 pptv lower for all months and reveals a distinct latitudinal gradient South from the tropical sites. In the FT there is very shallow cycle that is similar for WLG and LDR. But at STD-MAI peaks in January and July-August are observed. In the LS the lower latitude site at STD-MAI has the highest values through January to April then decreasing by as much as 70 pptv in September. LDR is similar but with a shallower amplitude. WLG sees a much lower mean value between 200-250 pptv. In the Antarctic, AHS sees considerable variability year over year in the LT and low values above 400 pptv that never are as low as in the Arctic e.g. EUR and TAB at 360 and 370 pptv in the autumn. Rather

AHS sees it highest FT values just before winter. FT values are very similar to southern mid-latitude values. But spring values are the lowest LS values seen at 160 pptv in September likely when subsidence still effects the LS. Summer and autumn values are consistent at about 240 pptv.

3.6 Latitudinal Variation

The latitudinal distribution of all mean OCS wVMR data are plotted in Figure 15. The upper panel are all data for each station and the lower panels are for each estimated monotonic trend period. Vertical bars represent $\pm 1\sigma$ and largely reflect the seasonal cycles shown in Figure 14. Owing to the tropospheric lifetime all free tropospheric mean values range higher than the lower tropospheric values, except between $0-20°$N where they are slightly reversed. This may point to a relatively larger net source in the Northern tropics as proposed e.g. Berry et al. (2013); Launois et al. (2015), though this is not seen further from the equator at IZA at 28°N. There are several stations between 30°N and 60°N that range from Japan, North America (NA) and Europe, where there is small decrease in OCS in the free troposphere and more so in lower troposphere. This persistent feature generally reproduces the in situ measurements given in Montzka et al. (2007) for NA, show that this effect is more global and may reflect a net continental sink.

Tropical sites show the highest stratospheric wVMR values between 300-360 pptv. These tend to fall in lower mid-latitudes than increase poleward in the NH where the Arctic sites maintain values of 300 - 310 pptv. There are fewer stations in the SH but the long-term site a AHS has a suppressed value of 220 pptv in the stratosphere.

3.7 Atmospheric Lifetime of OCS

Each site measures vertical profiles of N_2O as a standard data product as discussed with regards to dynamical proxies. Using tracer - tracer correlations for tropospheric source species that are in free tropospheric steady state with sinks only in the stratosphere as defined in Plumb and Ko (1992) and employed by Krysztofiak et al. (2015) the lifetime for LS OCS can be calculated with Eqn. 4.

$$\frac{\tau_{OCS}}{\tau_{N_2O}} = A \cdot \frac{wVMR_{OCS}}{wVMR_{N_2O}} \tag{4}$$

where τ is the respective species lifetime in years. Using monthly means, A is the linear correlation of the measured FT concentrations of N_2O and OCS using an orthogonal regression and propagating the uncertainties from the standard deviations of the monthly averages for both species. The wVMR are the respective measured LS monthly mixing ratios. The FT lifetime of N_2O used is (117 $\pm$ 20)y from Montzka and Fraser (2003). This was performed for all sites and binned by latitude as defined in Table 3. Calculations and results for the global estimate of LS OCS lifetime using all data are summarized in Table 8.

The latitudinal lifetime distribution show a clear increase poleward. At high latitudes the (84.5 $\pm$ 15.6)y calculated here is longer then the mean from several measurement sets of (71 $\pm$10)y found in Krysztofiak et al. (2015) although within error bars. The data here include 3 datasets at 76°N and higher latitudes which extend northward the reach from the previous balloon-borne datasets. The longest lifetime is recorded in the ($-50° - -90°$) zonal bin but composed of the single site at AHS.

4 Conclusions

This discussion seeks to show the long-term trends in OCS the largest reservoir of tropospheric sulfur and sulfuric source to the stratosphere where it plays an important role in maintaining the stratospheric sulphate aerosol layer. We presented atmospheric OCS time series data from 1986 (earliest) to 2020 from 22 globally distributed, from $80°N-79°S$, ground-based remote-sensing high-resolution NDACC FTIR stations. We developed a globally consistent retrieval analysis including measurement based a priori data to produce homogenous retrievals that were performed by each station managing group. These OCS vertical mixing ratio profiles were cast into partial columns and reduced to mean weighted mixing ratios then time averaged to represent mean monthly mixing ratios in the lower and free troposphere and lower stratosphere for globally consistent analysis.

This analysis showed that changes in trend on multi-year to decadal scales described in earlier reports are global features seen at other latitudes at stations with records of sufficient duration due to the long OCS lifetime. In particular the longest records at KIR, ZUG, JFJ, MLO, WLG and AHS show linear decreases from inception to the early 2000's revealed in the low and free tropospheric anomaly time series. Further, changes in trend are seen ~ 2008 and then in the $2016-2019$ period. To elucidate these changes we present linear trends during these periods in each altitude layer. We have obtained data for most stations up through 2019 or 2020. At about the 2016-2017 time period and later all stations show a down turn in trend in the free troposphere. This most recent linear time regime is short and limited conclusions should be drawn. But given the tropospheric lifetime of OCS of $\sim 2-3y$, if the tropospheric trend continues it may be realized in the stratosphere in the near future.

Two regressions were used to investigate the drivers of FT OCS concentration due to the time overlap of data and proxies. A two-step SMR approach defined important proxies and the COC correction accounted for the accumulation of OCS. Results show the relative the importance of SST at all zones, NDVI at northern hemisphere and tropical regions, MEI at northern high latitudes, and sea ice extent at northern high latitudes. Using SMR-COC approach, free tropospheric fluctuations of OCS are reproduced with an R^2 higher than 78% in most of the study sites though without COC R^2 ranged from 4 - 32%. Separately due to proxy and observational data overlap, free tropospheric time series at JFJ show a correlation with an $R^2 = 70\%$ with the revised anthropogenic emissions budget of Zumkehr et al. (2018) between 1986-2012. We would conclude this has had the largest effect on the LT and FT trends variability since 1986.

Stratospheric anomalies do not show the recent change since $\sim 2017 - 2019$. In the north and south mid-latitudes since 2008 increases are seen. At high northern latitudes there are small non-significant trends. AHS shows a positive change but with large uncertainty. This is in contrast to the negative trends at MLO and ALZ. Linear trends were calculated for the stratosphere with the anomaly data and by using retrieved N_2O stratospheric partial column data as a dynamical proxy. The comparison in trends for stations with records from 2001 - 2016 show a general improvement using the regression and slightly increased the trends with some exceptions. The trend at both WLG and LDR decreased. Nevertheless, globally northward of MLO and southward of WLG stratospheric trends have been increasing since 2001 0.12 to 0.32%/y and 0.27 to 0.79%/y respectively. This infers an excess of stratospheric sulfur over time and that the limiting factor to conversion to sulfate aerosol may not be sulfur derived from OCS. For the conditions of a steady state aerosol loading, the case may be more clear but given the uncertainty in total loading and its variability (Kremser et al., 2016) a stronger conclusion cannot be made from these observations.

Although this dataset is limited to 22 globally disperse locations, aside from the density of stations in continental Europe, the duration of the time series records and continuity of observations characterizes this as the most through global dataset of atmospheric carbonyl sulfide available. The dataset clearly show that the trend in OCS varies especially in the troposphere. That there is overall a small but increasing trend in the stratosphere seen in the longest time series except MLO 19.5°N and WLG at −34.4°S. Also that the trends in most of the atmosphere was increasing in the period 2008−2016 but that this trend seen in the tropospheric data to 2020 is now decreasing at all stations.

Finally these data currently will become a standard NDACC IRWG data product, will be archived at the NDACC DHF and available to the public.

Acknowledgments

The National Center for Atmospheric Research is sponsored by the National Science Foundation. The NCAR FTS observation programs at Thule, GR, Boulder, CO and Mauna Loa, HI are supported under contract by the National Aeronautics and Space Administration (NASA). The Thule work is also supported by the NSF Office of Polar Programs (OPP). We wish to thank the Danish Meteorological Institute for support at the Thule site and NOAA for support at the MLO site.

The Eureka measurements were made at the Polar Environment Atmospheric Research Laboratory (PEARL) by the Canadian Network for the Detection of Atmospheric Change (CANDAC), and the Toronto measurements were made at the University of Toronto Atmospheric Observatory (TAO); both are primarily supported by the Natural Sciences and Engineering Research Council of Canada (NSERC), the Canadian Space Agency (CSA), and Environment and Climate Change Canada (ECCC).

The Paris station has received funding from Sorbonne Université, the French research center CNRS, the French space agency CNES, and Région Île-de-France.

The Jungfraujoch FTIR monitoring program has received funding from the F.R.S.-FNRS (under grants J.0147.18 and J.0126.21), the Fédération Wallonie-Bruxelles, both in Brussels, Belgium, and from the GAW-CH program of MeteoSwiss. EM is a senior research associate with F.R.S.-FNRS.

Alejandro Bezanilla is acknowledged for measurements and data managements of the Altzomoni Site and Alfredo Rodriguez, Delibes Flores, Omar Lopez, and Eugenia Gonzalez de Castillo are acknowledged for technical support. The Observations in Mexico are founded by the grants CONACYT-290589 and PAPIIT-IN111521. RUOA-Network `https://www.ruoa.unam.mx/` is acknowledged by supporting the infrastructure of the Altzomoni Observatory and the administration of the National Park Izta-Popo Zoquiapan are acknowledged for hosting and supporting this site.

KIT, IMK-ASF would like to thank Uwe Raffalski and Peter Voelger from the Swedish Institute of Space Physics (IRF) for their continuing support of the NDACC FTIR site Kiruna.

FTIR measurements at Lauder and Arrival Heights are core-funded by NIWA (programme CAAC_2201) through New Zealand's Ministry of Business, Innovation and Employment Strategic Science Investment Fund. We also thank Antarctica New Zealand for providing logistical support for the FTIR measurements at Arrival Heights.

The University of Bremen team acknowledge the AWI Bremerhaven,Germany, and the personnel at the AWIPEV research base in Ny Ålesund, Svalbard, for logistical and on-site support. This publication has been supported by the senate of Bremen, the BMBF (Federal Ministry of Education and Research, Germany) in the ROMIC-II subproject TroStra (FKZ: 01LG1904A) and the DFG (German research foundation in the Transregio 172, Arctic Amplification, project number 268020496, subproject E02).

The Izaña FTIR station has been supported by the German Bundesministerium für Wirtschaft und Energie (BMWi) via DLRunder grants 50EE1711A and by the Helmholtz Society via the research program ATMO.

Operation at the Rikubetsu and Tsukuba sites are supported in part by the GOSAT series project. Analyses of the Rikubetsu and Tsukuba data were carried out as part of the ISEE joint research program.

The University of Wollongong operates the NDACC site at Wollongong and is funded through grants from the Australian Research Council.

The NDACC FTIR station Zugspitze has been supported by the German Bundesministerium für Wirtschaft und Energie (BMWi) via DLR under grant 50EE1711D and by the Helmholtz Society via the research program ATMO.

The measurements at Reunion Island have been also supported by the Université de La Réunion and CNRS (LACy-UMR8105 and UMS3365).

FTIR data of SPbU were acquired using instrumentation facilities provided by the Geomodel Research Center of SPbU Research Park.

The authors wish to thank S. Kremser (Bodeker Scientific Inc.) for many useful conversations concerning OCS and stratospheric aerosols.

References

Appenzeller, C., Weiss, A. K., & Staehelin, J. (2000). North atlantic oscillation modulates total ozone winter trends. *Geophysical Research Letters*, *27*(8), 1131-1134. Retrieved from `https://agupubs.onlinelibrary.wiley.com/doi/abs/10.1029/1999GL010854` doi: https://doi.org/10.1029/1999GL010854

Bahramvash Shams, S., Walden, V. P., Petropavlovskikh, I., Tarasick, D., Kivi, R., Oltmans, S., ... Errera, Q. (2019). Variations in the vertical profile of ozone at four high-latitude arctic sites from 2005 to 2017. *Atmospheric Chemistry and Physics*, *19*(15), 9733–9751. Retrieved from `https://acp.copernicus.org/articles/19/9733/2019/` doi: 10.5194/acp-19-9733-2019

Barkley, M. P., Palmer, P. I., Boone, C. D., Bernath, P. F., & Suntharalingam, P. (2008). Global distributions of carbonyl sulfide in the upper troposphere and stratosphere. *Geophysical Research Letters*, *35*(14), n/a–n/a. Retrieved from `http://dx.doi.org/10.1029/2008GL034270` (L14810) doi: 10.1029/2008GL034270

Becagli, S., Lazzara, L., Marchese, C., Dayan, U., Ascanius, S., Cacciani, M., ... Udisti, R. (2016). Relationships linking primary production, sea ice melting, and biogenic aerosol in the Arctic. *Atmospheric Environment*, *136*, 1-15. Retrieved from `http://www.sciencedirect.com/science/article/pii/S135223101630259X` doi: https://doi.org/10.1016/j.atmosenv.2016.04.002

Berry, J., Wolf, A., Campbell, J. E., Baker, I., Blake, N., Blake, D., ... Zhu, Z. (2013, April). A coupled model of the global cycles of carbonyl sulfide and co2: A possible new window on the carbon cycle. *Journal of Geophysical Research: Biogeosciences*, *118*(2), 842–852. Retrieved from `https://doi.org/10.1002/jgrg.20068` doi: 10.1002/jgrg.20068

Boone, C. D., Walker, K. A., & Bernath, P. F. (2013, 01). Version 3 retrievals for the atmospheric chemistry experiment fourier transform spectrometer (ace-fts). In *The atmospheric chemistry experiment ace at 10: A solar occultation anthology* (p. 103-127). (Peter F. Bernath, editor, A. Deepak Publishing, Hampton, Virginia, U.S.A., 2013).

Brühl, C., Lelieveld, J., Crutzen, P. J., & Tost, H. (2012). The role of carbonyl sulphide as a source of stratospheric sulphate aerosol and its impact on climate. *Atmospheric Chemistry and Physics*, *12*(3), 1239–1253. Retrieved from `https://www.atmos-chem-phys.net/12/1239/2012/` doi: 10.5194/acp-12-1239-2012

Brunner, D., Staehelin, J., Maeder, J. A., Wohltmann, I., & Bodeker, G. E. (2006). Variability and trends in total and vertically resolved stratospheric ozone based on the cato ozone data set. *Atmospheric Chemistry and Physics*, *6*(12), 4985–5008. Retrieved from `http://www.atmos-chem-phys.net/6/4985/2006/` doi: 10.5194/acp-6-4985-2006

Buchholz, R. R., Deeter, M. N., Worden, H. M., Gille, J., Edwards, D. P., Hannigan, J. W., ... Langerock, B. (2017, 6). Validation of MOPITT carbon monoxide using ground-based Fourier transform infrared spectrometer data from NDACC. *Atmospheric Measurement Techniques*, *10*(5), 1927–1956. Retrieved from `http://www.atmos-meas-tech.net/10/1927/2017/` doi: 10.5194/amt-10-1927-2017

Campbell, J. E., Berry, J. A., Seibt, U., Smith, S. J., Montzka, S. A., Launois, T., ... Laine, M. (2017, 04 05). Large historical growth in global terrestrial gross primary production. *Nature*, *544*, 84-87. Retrieved from `http://dx.doi.org/10.1038/nature22030`

Campbell, J. E., Whelan, M. E., Seibt, U., Smith, S. J., Berry, J. A., & Hilton, T. W. (2015). Atmospheric carbonyl sulfide sources from anthropogenic activity: Implications for carbon cycle constraints. *Geophysical Research Letters*, *42*(8), 3004-3010. Retrieved from `https://agupubs.onlinelibrary.wiley.com/doi/abs/10.1002/2015GL063445` doi: https://doi.org/10.1002/2015GL063445

Cochrane, D., & Orcutt, G. H. (1949). Application of least squares regression to relationships containing auto- correlated error terms. *Journal of the American*

Statistical Association, *44*(245), 32–61. Retrieved from http://www.jstor.org/stable/2280349

Coffey, M. T., & Hannigan, J. W. (2010). The Temporal Trend of Stratospheric Carbonyl Sulfide. *Journal of Atmospheric Chemistry*, *67*, 61 – 70. doi: 10.1007/s10874-011-9203-4

Crutzen, P. J. (1976, February). The possible importance of CSO for the sulfate layer of the stratosphere. *Geophysical Research Letters*, *3*, 73-76. doi: 10.1029/GL003i002p00073

Dammers, E., Shephard, M. W., Palm, M., Cady-Pereira, K., Capps, S., Lutsch, E., ... Erisman, J. W. (2017, 7). Validation of the CrIS fast physical NH_3 retrieval with ground-based FTIR. *Atmospheric Measurement Techniques*, *10*(7), 2645–2667. Retrieved from https://www.atmos-meas-tech.net/10/2645/2017/ doi: 10.5194/amt-10-2645-2017

De Mazière, M., Thompson, A. M., Kurylo, M. J., Wild, J. D., Bernhard, G., Blumenstock, T., ... Strahan, S. E. (2018, 4). The Network for the Detection of Atmospheric Composition Change (NDACC): history, status and perspectives. *Atmospheric Chemistry and Physics*, *18*(7), 4935–4964. Retrieved from https://www.atmos-chem-phys.net/18/4935/2018/ doi: 10.5194/acp-18-4935-2018

Eyring, V., Waugh, D. W., G. E. Bodeker, . E. C., Akiyoshi, H., Austin, J., Beagley, S. R., ... Yoshiki, M. (2007). Multimodel projections of stratospheric ozone in the 21st century. *J. Geophys. Res*, *112*(D16303). doi: 10.1029/2006JD00833

Finger, F. G., Gelman, M. E., Miller, A. J., Wild, J. D., Chanin, M. L., & Hauchecorne, A. (1993, March). Evaluation of nmc upper-stratospheric temperature analyses using rocketsonde and lidar data. *Bulletin of the American Meteorological Society*, *74*(5), 789–799. Retrieved from http://dx.doi.org/10.1175/1520-0477(1993)074<0789:EONUST>2.0.CO;2 doi: 10.1175/1520-0477(1993)074⟨0789:EONUST⟩2.0.CO;2

Garcia, R. R., Marsh, D. R., Kinnison, D. E., Boville, B. A., & Sassi, F. (2007). Simulation of secular trends in the middle atmosphere, 1950–2003. *J. Geophys. Res*, *112*(D09301). doi: 10.1029/2006JD007485

Gardiner, T., Forbes, A., de Mazière, M., Vigouroux, C., Mahieu, E., Demoulin, P., ... Gauss, M. (2008). Trend analysis of greenhouse gases over europe measured by a network of ground-based remote ftir instruments. *Atmospheric Chemistry and Physics*, *8*(22), 6719–6727. Retrieved from http://www.atmos-chem-phys.net/8/6719/2008/ doi: 10.5194/acp-8-6719-2008

Gaudel, A., Cooper, O. R., Ancellet, G., Barret, B., Boynard, A., Burrows, J. P., . . . Lewis, A. (2018). Tropospheric ozone assessment report: Present-day distribution and trends of tropospheric ozone relevant to climate and global atmospheric chemistry model evaluation. *Elem Sci Anth*, *6*. Retrieved from https://doi.org/10.1525/elementa.291 doi: 10.1525/elementa.291

Glatthor, N., Höpfner, M., Leyser, A., Stiller, G. P., von Clarmann, T., Grabowski, U., . . . Walker, K. A. (2017). Global carbonyl sulfide (OCS) measured by MIPAS/Envisat during 2002-2012. *Atmospheric Chemistry and Physics*, *17*(4), 2631–2652. Retrieved from http://www.atmos-chem-phys.net/17/2631/2017/ doi: 10.5194/acp-17-2631-2017

Griffith, D. W. T., Jones, N. B., & Matthews, W. A. (1998, Apr). Interhemispheric ratio and annual cycle of carbonyl sulfide (ocs) total column from ground-based solar ftir spectra. *Journal of Geophysical Research: Atmospheres*, *103*(D7), 8447–8454. Retrieved from https://doi.org/10.1029/97JD03462 doi: 10.1029/97JD03462

Gunson, M. R., Abbas, M. M., Abrams, M. C., Allen, M., Brown, L. R., Brown, T. L., . . . Zander, R. (1996). The atmospheric trace molecule spectroscopy (atmos) experiment: Deployment on the atlas space shuttle missions. *Geophysical Research Letters*, *23*(17), 2333-2336. Retrieved from https://agupubs.onlinelibrary.wiley.com/doi/abs/10.1029/96GL01569 doi: https://doi.org/10.1029/96GL01569

Hase, F. (2000). *Inversion von Spurengasprofilen aus hochaufgelösten bodengebundenen FTIR-Messungen in Absorption* (Unpublished doctoral dissertation). Fakultät für Physik der Universität Karlsruhe.

Hase, F., Hannigan, J., Coffey, M., Goldman, A., Höpfner, M., Jones, N., . . . Wood, S. (2004). Intercomparison of retrieval codes used for the analysis of high-resolution, ground-based FTIR measurements. *Journal of Quantitative Spectroscopy and Radiative Transfer*, *87*, 24 – 52. doi: 10.1016/j.jqsrt.2003.12.008

Hilton, T. W., Whelan, M. E., Zumkehr, A., Kulkarni, S., Berry, J. A., Baker, I. T., . . . Elliott Campbell, J. (2017). Peak growing season gross uptake of carbon in north america is largest in the midwest usa. *Nature Climate Change*, *7*(6), 450–454. Retrieved from `https://doi.org/10.1038/nclimate3272` doi: 10.1038/nclimate3272

Kettle, A. J., Kuhn, U., von Hobe, M., Kesselmeier, J., & Andreae, M. O. (2002, November). Global budget of atmospheric carbonyl sulfide: Temporal and spatial variations of the dominant sources and sinks. *Journal of Geophysical Research (Atmospheres)*, *107*, 4658. doi: 10.1029/2002JD002187

Kivi, R., Kyrö, E., Turunen, T., Harris, N. R. P., von der Gathen, P., Rex, M., … Wohltmann, I. (2007). Ozonesonde observations in the arctic during 1989–2003: Ozone variability and trends in the lower stratosphere and free troposphere. *Journal of Geophysical Research: Atmospheres*, *112*(D8). Retrieved from `https://agupubs.onlinelibrary.wiley.com/doi/abs/10.1029/2006JD007271` doi: https://doi.org/10.1029/2006JD007271

Kohlhepp, R., Ruhnke, R., Chipperfield, M. P., De Mazière, M., Notholt, J., Barthlott, S., … Wood, S. W. (2012). Observed and simulated time evolution of HCl, $ClONO_2$, and HF total column abundances. *Atmospheric Chemistry & Physics*, *12*(7), 3527–3556. Retrieved from `http://www.atmos-chem-phys.net/12/3527/2012/` doi: 10.5194/acp-12-3527-2012

Kremser, S., Jones, N. B., Palm, M., Lejeune, B., Wang, Y., Smale, D., & Deutscher, N. M. (2015). Positive trends in Southern Hemisphere carbonyl sulfide. *Geophysical Research Letters*, *42*(21), 9473–9480. Retrieved from `http://dx.doi.org/10.1002/2015GL065879` (2015GL065879) doi: 10.1002/2015GL065879

Kremser, S., Thomason, L. W., von Hobe, M., Hermann, M., Deshler, T., Timmreck, C., … Meland, B. (2016, Mar). Stratospheric aerosol—observations, processes, and impact on climate. *Reviews of Geophysics*, *54*(2), 278–335. Retrieved from `https://doi.org/10.1002/2015RG000511` doi: 10.1002/2015RG000511

Krysztofiak, G., Té, Y. V., Catoire, V., Berthet, G., Toon, G. C., Jégou, F., … Robert, C. (2015). Carbonyl Sulphide (OCS) Variability with Latitude in the Atmosphere. *Atmosphere-Ocean*, *53*(1), 89-101. Retrieved from `http://dx.doi.org/10.1080/07055900.2013.876609` doi: 10.1080/07055900.2013.876609

Kurylo, M. J., & Soloman, S. (1990). *United states nasa administration upper atmo-*

sphere research program and noaa climate and global change program, network for the detection of stratospheric change: a status and implementation report. (Tech. Rep.). NASA, Washington, D.C.

Launois, T., Belviso, S., Bopp, L., Fichot, C. G., & Peylin, P. (2015). A new model for the global biogeochemical cycle of carbonyl sulfide - Part 1: Assessment of direct marine emissions with an oceanic general circulation and biogeochemistry model. *Atmospheric Chemistry and Physics*, *15*(5), 2295–2312. Retrieved from `http://www.atmos-chem-phys.net/15/2295/2015/` doi: 10.5194/acp-15-2295-2015

Lee, C.-L., & Brimblecombe, P. (2016). Anthropogenic contributions to global carbonyl sulfide, carbon disulfide and organosulfides fluxes. *Earth-Science Reviews*, *160*, 1 - 18. Retrieved from `http://www.sciencedirect.com/science/article/pii/S0012825216301210` doi: http://dx.doi.org/10.1016/j.earscirev.2016.06.005

Lejeune, B., Mahieu, E., Vollmer, M. K., Reimann, S., Bernath, P. F., Boone, C. D., ... Servais, C. (2016, Jan). Optimized approach to retrieve information on atmospheric carbonyl sulfide (OCS) above the Jungfraujoch station and change in its abundance since 1995. *Journal of Quantitative Spectroscopy & Radiative Transfer*, *186*, 81-95. Retrieved from `http://www.sciencedirect.com/science/article/pii/S0022407316300899` doi: http://dx.doi.org/10.1016/j.jqsrt.2016.06.001

Ma, J., Kooijmans, L. M. J., Cho, A., Montzka, S. A., Glatthor, N., Worden, J. R., ... Krol, M. C. (2020). Inverse modelling of carbonyl sulfide: implementation, evaluation and implications for the global budget. *Atmospheric Chemistry and Physics Discussions*, *2020*, 1–39. Retrieved from `https://www.atmos-chem-phys-discuss.net/acp-2020-603/` doi: 10.5194/acp-2020-603

Mahieu, E., Zander, R., Delbouille, L., Demoulin, P., Roland, G., & Servais, C. (1997, NOV). Observed trends in total vertical column abundances of atmospheric gases from IR solar spectra recorded at the Jungfraujoch [Article]. *JOURNAL OF ATMOSPHERIC CHEMISTRY*, *28*(1-3), 227-243. doi: {10.1023/A:1005854926740}

Mankin, W. G., Coffey, M. T., Griffith, D. W. T., & Drayson, S. R. (1979, November). Spectroscopic measurement of carbonyl sulfide (OCS) in the stratosphere. *Geophysical Research Letters*, *6*, 853-856. doi: 10.1029/GL006i011p00853

Montzka, S. A., Calvert, P., Hall, B. D., Elkins, J. W., Conway, T. J., Tans, P. P., & Sweeney, C. (2007). On the global distribution, seasonality, and budget of atmospheric carbonyl sulfide (COS) and some similarities to CO2. *Journal of Geophysical Research: Atmospheres*, *112*(D9). Retrieved from `http://dx.doi.org/10.1029/2006JD007665` (D09302) doi: 10.1029/2006JD007665

Notholt, J., Bingemer, H., Berresheim, H., Holton, J., Kettle, A., Mahieu, E., ... edited by L. Thomason and T. Peter (2006). Precursor gas measurements, in SPARC Assessment of Aerosol Processes (ASAP). In (p. 29-76). Geneva, Switzerland: World Climate Research Programme.

Notholt, J., Kuang, Z., Rinsland, C. P., Toon, G. C., Rex, M., Jones, N., ... Schrems, O. (2003). Enhanced Upper Tropical Tropospheric COS: Impact on the Stratospheric Aerosol Layer. *Science*, *300*(5617), 307-310. Retrieved from `http://www.sciencemag.org/content/300/5617/307.abstract` doi: 10.1126/science.1080320

Olsen, K. S., Strong, K., Walker, K. A., Boone, C. D., Raspollini, P., Plieninger, J., ... Saitoh, N. (2017, 10). Comparison of the GOSAT TANSO-FTS TIR CH_4 volume mixing ratio vertical profiles with those measured by ACE-FTS, ESA MIPAS, IMK-IAA MIPAS, and 16 NDACC stations. *Atmospheric Measurement Techniques*, *10*(10), 3697–3718. Retrieved from `https://www.atmos-meas-tech.net/10/3697/2017/` doi: 10.5194/amt-10-3697-2017

Plumb, R. A., & Ko, M. K. W. (1992, Jun). Interrelationships between mixing ratios of long-lived stratospheric constituents. *Journal of Geophysical Research: Atmospheres*, *97*(D9), 10145–10156. Retrieved from `https://doi.org/10.1029/92JD00450` doi: 10.1029/92JD00450

Pougatchev, N. S., Connor, B. J., & Rinsland, C. P. (1995). Infrared measurements of the ozone vertical distribution above kitt peak. *Journal of Geophysical Research: Atmospheres*, *100*(D8), 16689–16697. Retrieved from `http://dx.doi.org/10.1029/95JD01296` doi: 10.1029/95JD01296

Randel, W. J., Shine, K. P., Austin, J., Barnett, J., Claud, C., Gillett, N. P., ... Yoden, S. (2009). An update of observed stratospheric temperature trends. *J.*

Geophys. Res, *114*(D02107). doi: 10.1029/2008JD010421

Rinsland, C. P., Chiou, L., Mahieu, E., Zander, R., Boone, C. D., & Bernath, P. F. (2008). Measurements of long-term changes in atmospheric OCS (carbonyl sulfide) from infrared solar observations. *J. Quant. Spectrosc. Radiat. Transfer*, *109*, 2679 – 2686. doi: 10.1016/j.jqsrt.2008.07.008

Rinsland, C. P., Goldman, A., Mahieu, E., Zander, R., Notholt, J., Jones, N. B., … Chiou, L. S. (2002). Ground-based infrared spectroscopic measurements of carbonyl sulfide: Free tropospheric trends from a 24-year time series of solar absorption measurements. *Journal of Geophysical Research: Atmospheres*, *107*(D22), ACH 24-1–ACH 24-9. Retrieved from `https://doi.org/10.1029/2002JD002522` doi: 10.1029/2002JD002522

Rinsland, C. P., Jones, N. B., Connor, B. J., Logan, J. A., Pougatchev, N. S., Goldman, A., … Demoulin, P. (1998). Northern and southern hemisphere ground-based infrared spectroscopic measurements of tropospheric carbon monoxide and ethane. *Journal of Geophysical Reasearch*, *103*, 28,197-28,217.

Rodgers, C. D. (1976, Nov). Retrieval of atmospheric temperature and composition from remote measurements of thermal radiation. *Reviews of Geophysics*, *14*(4), 609–624. Retrieved from `https://doi.org/10.1029/RG014i004p00609` doi: 10.1029/RG014i004p00609

Rodgers, C. D. (1990, Apr). Characterization and error analysis of profiles retrieved from remote sounding measurements. *Journal of Geophysical Research: Atmospheres*, *95*(D5), 5587–5595. Retrieved from `https://doi.org/10.1029/JD095iD05p05587` doi: 10.1029/JD095iD05p05587

Rodgers, C. D. (1998). Information content and optimisation of high spectral resolution remote measurements. *Adv. Space Res.*, *21*, 361-367.

Rodgers, C. D. (2000). *Inverse methods for atmospheric sounding.* World Scientific Publishing Co. Pte. Ltd.

Rothman, L., Gordon, I., Babikov, Y., Barbe, A., Benner, D. C., Bernath, P., … Wagner, G. (2013, July). The HITRAN 2012 molecular spectroscopic database. *Journal of Quantitative Spectroscopy and Radiative Transfer*, *130*(0), 4-50. Retrieved from `http://www.sciencedirect.com/science/article/pii/S0022407313002859` doi: http://dx.doi.org/10.1016/j.jqsrt.2013.07.002

Sheng, J.-X., Weisenstein, D. K., Luo, B.-P., Rozanov, E., Stenke, A., Anet, J., . . . Peter, T. (2015, Mar). Global atmospheric sulfur budget under volcanically quiescent conditions: Aerosol-chemistry-climate model predictions and validation. *Journal of Geophysical Research: Atmospheres*, *120*(1), 256–276. Retrieved from https://doi.org/10.1002/2014JD021985 doi: 10.1002/2014JD021985

Stinecipher, J., Cameron-Smith, P., Blake, N., Kuai, L., Lejeune, B., Mahieu, E., . . . Campbell, J. (2019). Biomass burning unlikely to account for missing source of carbonyl sulfide. *Geophysical Research Letters*, *46*(24), 14912-14920. Retrieved from https://agupubs.onlinelibrary.wiley.com/doi/abs/10.1029/2019GL085567 doi: https://doi.org/10.1029/2019GL085567

Stolarski, R. S., Douglass, A. R., & Strahan, S. E. (2018). Using satellite measurements of n_2o to remove dynamical variability from hcl measurements. *Atmospheric Chemistry and Physics*, *18*(8), 5691–5697. Retrieved from https://www.atmos-chem-phys.net/18/5691/2018/ doi: 10.5194/acp-18-5691-2018

Suntharalingam, P., Kettle, A. J., Montzka, S. M., & Jacob, D. J. (2008). Global 3-D model analysis of the seasonal cycle of atmospheric carbonyl sulfide: Implications for terrestrial vegetation uptake. *Geophys. Res. Lett.*, *35*, L19801. doi: 10.1029/2008GL034332

Thomason, L., & Peter, T. (2006). *SPARC Assessment of Aerosol Processes (ASAP)* (Tech. Rep.). Geneva, Switzerland: World Climate Research Programme.

Toon, G. C., Blavier, J.-F. L., & Sung, K. (2018). Atmospheric carbonyl sulfide (ocs) measured remotely by ftir solar absorption spectrometry. *Atmospheric Chemistry and Physics*, *18*(3), 1923–1944. Retrieved from https://www.atmos-chem-phys.net/18/1923/2018/ doi: 10.5194/acp-18-1923-2018

Turco, R. P., Whitten, R. C., Toon, O. B., Pollack, J. B., & Hamill, P. (1980, 01 17). Ocs, stratospheric aerosols and climate. *Nature*, *283*(5744), 283–285. Retrieved from http://dx.doi.org/10.1038/283283a0

Velazco, V. A., Toon, G. C., Blavier, J.-F. L., Kleinböhl, A., Manney, G. L., Daffer, W. H., . . . Boone, C. (2011). Validation of the Atmospheric Chemistry Experiment by noncoincident MkIV balloon profiles. *Journal of Geophysical Research: Atmospheres*, *116*(D6), n/a–n/a. Retrieved from http://dx.doi.org/10.1029/2010JD014928 (D06306) doi:

10.1029/2010JD014928

Vigouroux, C., Aquino, C. A. B., Bauwens, M., Becker, C., Blumenstock, T., Mazière, M. D., ... Toon, G. (2018, 9). NDACC harmonized formaldehyde time-series from 21 FTIR stations covering a wide range of column abundances. *Atmospheric Measurement Techniques*, *11*(9), 5049–5073. doi: {10.5194/amt-11-5049-2018}

Vigouroux, C., Blumenstock, T., Coffey, M., Errera, Q., García, O., Jones, N. B., ... De Mazière, M. (2015). Trends of ozone total columns and vertical distribution from FTIR observations at eight NDACC stations around the globe. *Atmospheric Chemistry & Physics*, *15*(6), 2915–2933. Retrieved from http://www.atmos-chem-phys.net/15/2915/2015/ doi: 10.5194/acp-15-2915-2015

Vigouroux, C., Mazière, M. D., Demoulin, P., Servais, C., Hase, F., Blumenstock, T., ... Woods, P. (2008). Evaluation of tropospheric and stratospheric ozone trends over Western Europe from ground-based FTIR network observations. *Atmos. Chem. Phys.*, *8*, 6865 – 6886. Retrieved from www.atmos-chem-phys.net/8/6865/2008/

Wang, Y., Deutscher, N. M., Palm, M., Warneke, T., Notholt, J., Baker, I., ... Kremser, S. (2016, 2). Towards understanding the variability in biospheric CO2 fluxes: using FTIR spectrometry and a chemical transport model to investigate the sources and sinks of carbonyl sulfide and its link to CO_2. *Atmospheric Chemistry and Physics*, *16*(4), 2123–2138. Retrieved from http://www.atmos-chem-phys.net/16/2123/2016/ doi: 10.5194/acp-16-2123-2016

Whelan, M. E., Lennartz, S. T., Gimeno, T. E., Wehr, R., Wohlfahrt, G., Wang, Y., ... Campbell, J. E. (2018, 1). Reviews and syntheses: Carbonyl sulfide as a multi-scale tracer for carbon and water cycles. *Biogeosciences*, *15*(12), 3625–3657. Retrieved from https://www.biogeosciences.net/15/3625/2018/ doi: 10.5194/bg-15-3625-2018

Wild, J. D., Gelman, M. E., Miller, A. J., Chanin, M. L., Hauchecorne, A., Keckhut, P., ... Fishbein, E. F. (1995, Jan). Comparison of stratospheric temperatures from several lidars, using national meteorological center and microwave limb sounder data as transfer references. *Journal of Geo-*

physical Research: Atmospheres, *100*(D6), 11105–11111. Retrieved from https://doi.org/10.1029/95JD00631 doi: 10.1029/95JD00631

Wilks, D. S. (2011). *Statistical methods in the atmospheric sciences* (3rd ed.). Elsevier, Oxford.

Wofsy, S. C. (2011). Hiaper pole-to-pole observations (hippo): fine-grained, global-scale measurements of climatically important atmospheric gases and aerosols. *Philosophical Transactions of the Royal Society of London A: Mathematical, Physical and Engineering Sciences*, *369*(1943), 2073–2086. Retrieved from http://rsta.royalsocietypublishing.org/content/369/1943/2073 doi: 10.1098/rsta.2010.0313

Wofsy, S. C., Daube, B. C., Jimenez, R., Kort, E., Pittman, J. V., Park, S., … Mahoney, M. J. (2017). *HIPPO Combined Discrete Flask and GC Sample GHG, Halocarbon, Hydrocarbon Data Version 1.0. (R20121129)* (Tech. Rep.). UCAR/NCAR - Earth Observing Laboratory, Boulder, CO, U.S.A. doi: http://dx.doi.org/10.3334/CDIAC/hippo_012

Wohltmann, I., Lehmann, R., Rex, M., Brunner, D., & Mäder, J. A. (2007). A process-oriented regression model for column ozone. *Journal of Geophysical Research: Atmospheres*, *112*(D12). Retrieved from https://agupubs.onlinelibrary.wiley.com/doi/abs/10.1029/2006JD007573 doi: https://doi.org/10.1029/2006JD007573

Zander, R., Rinsland, C. P., Farmer, C. B., Namkung, J., Norton, R. H., & Russell III, J. M. (1988). Concentrations of carbonyl sulfide and hydrogen cyanide in the free upper troposphere and lower stratosphere deduced from atmos/spacelab 3 infrared solar occultation spectra. *Journal of Geophysical Research: Atmospheres*, *93*(D2), 1669-1678. Retrieved from https://agupubs.onlinelibrary.wiley.com/doi/abs/10.1029/JD093iD02p01669 doi: https://doi.org/10.1029/JD093iD02p01669

Zängl, G., & Hoinka, K. P. (2001). The tropopause in the polar regions. *Journal of Climate*, *14*(14), 3117-3139. Retrieved from http://dx.doi.org/10.1175/1520-0442(2001)014<3117:TTITPR>2.0.CO;2 doi: 10.1175/1520-0442(2001)014⟨3117:TTITPR⟩2.0.CO;2

Zhou, M., Langerock, B., Wells, K. C., Millet, D. B., Vigouroux, C., Sha, M. K., … De Mazière, M. (2019). An intercomparison of total column-averaged

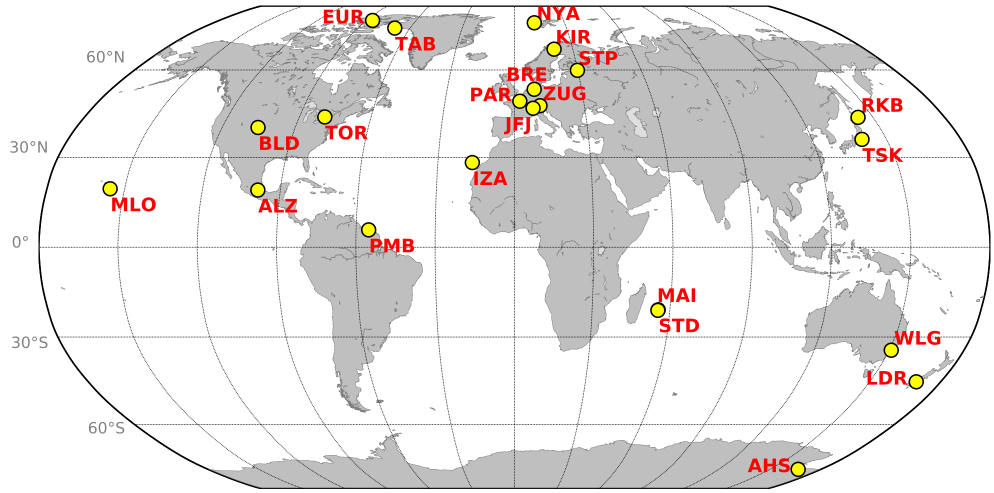

Figure 1. *Global map of NDACC FTIR stations contributing to this study. Note PAR is not currently a formal NDACC station.*

nitrous oxide between ground-based FTIR TCCON and NDACC measurements at seven sites and comparisons with the GEOS-Chem model. *Atmospheric Measurement Techniques*, *12*(2), 1393–1408. Retrieved from `https://www.atmos-meas-tech.net/12/1393/2019/` doi: 10.5194/amt-12-1393-2019

Zumkehr, A., Hilton, T. W., Whelan, M., Smith, S., Kuai, L., Worden, J., & Campbell, J. E. (2018). Global gridded anthropogenic emissions inventory of carbonyl sulfide. *Atmospheric Environment*, *183*, 11 - 19. Retrieved from `http://www.sciencedirect.com/science/article/pii/S1352231018302255` doi: https://doi.org/10.1016/j.atmosenv.2018.03.063

Table 1. *Stations contributing to OCS analysis. Station abbreviation, station location name, location coordinates, and managing institution.*

Station	Location	N. Lat.	E. Lon.	m.a.s.l.	Managing Institution
EUR	Eureka	80.05	273.58	610	U. Toronto
NYA	Ny Ålesund	78.90	11.90	20	U. Bremen
TAB	Thule	76.53	291.26	225	NCAR
KIR	Kiruna	67.84	20.41	420	KIT-ASF
STP	St Petersburg	59.88	29.83	20	U. St. Petersburg
BRE	Bremen	53.10	8.90	27	U. Bremen
PAR	Paris	48.97	2.37	60	LERMA
ZUG	Zugspitze	47.42	10.98	2964	KIT-IFU
JFJ	Jungfraujoch	46.55	7.98	3580	U. Liège
TOR	Toronto	43.66	280.60	174	U. Toronto
RKB	Rikubetsu	43.46	143.77	380	U. Nagoya
BLD	Boulder	40.04	254.76	1612	NCAR
TSK	Tsukuba	36.05	140.12	31	NIES
IZA	Izaña	28.30	343.52	2370	KIT-ASF
MLO	Mauna Loa	19.54	204.43	3396	NCAR
ALZ	Altzomoni	19.12	261.35	4010	UNAM
PAR	Paramaribo	5.81	304.79	7	U. Bremen
MAI	Reunion Is. Maïdo	-21.07	55.38	2160	BIRA
STD	Reunion Is. St. Denis	-21.09	55.48	50	BIRA
WLG	Wollongong	-34.41	150.88	30	U. Wollongong
LDR	Lauder	-45.05	169.67	370	NIWA
AHS	Arrival Heights	-78.83	166.66	200	NIWA

Table 2. *Spectral regions, OCS absorption features and possible interfering species used for the Optimal Estimation retrieval of OCS.*

Microwindow [cm^{-1}]	OCS Absorption Line	Interfering Species
1) 2030.75 - 2031.06 (Optional)	-	CO_2, O_3
2) 2047.85 - 2048.24	P(32)	OCS, CO_2, O_3
3) 2049.77 - 2050.18	P(28)	OCS, H_2O, $^{12}C^{16}O^{18}O$, O_3, CO
4) 2054.33 - 2054.67	P(18)	OCS, H_2O, $H_2^{18}O$, CO_2, O_3

Table 3. *Number of profiles used from each HIPPO and ACE-FTS dataset by latitude bin required for a priori consistency.*

Latitude bin	HIPPO Surface - 14km	ACE-FTS 14km -30km
50.0 - 90.0	17	12577
20.0 - 50.0	12	2830
-20.0 - 20.0	11	1957
-50.0 - -20.0	11	2536
-90.0 - -50.0	5	12125

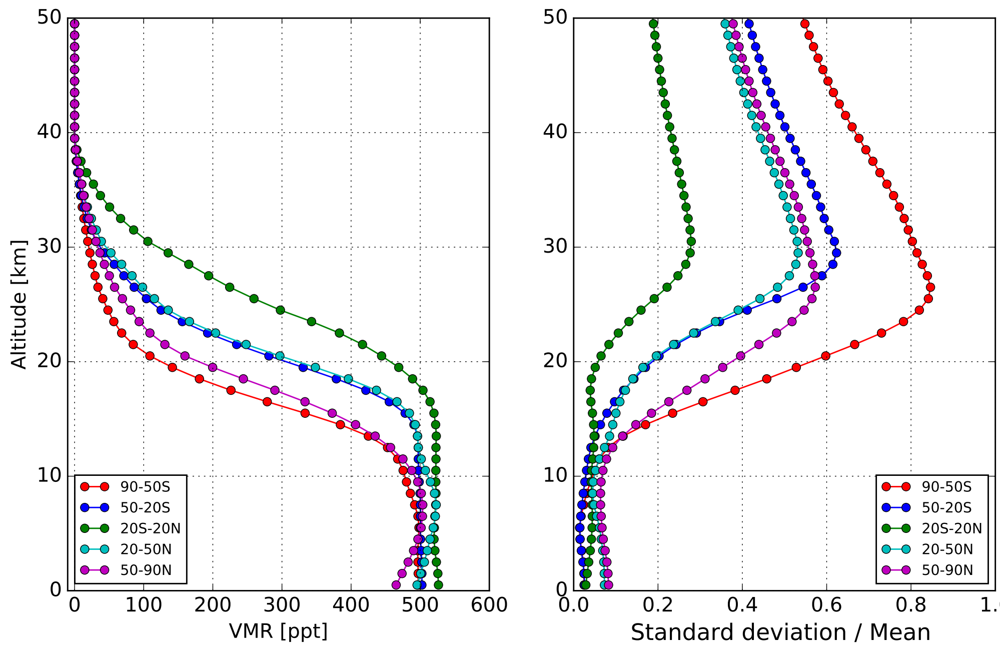

Figure 2. *A priori vertical profiles of OCS binned by latitudes as in Table 3 derived from concatenated and smoothed global HIPPO and ACE-FTS data. In the left panel are the observation based a priori profiles as described in the text. In the right panel are the standard deviation from all profiles for that bin used for the S_a covariance, see text for details.*

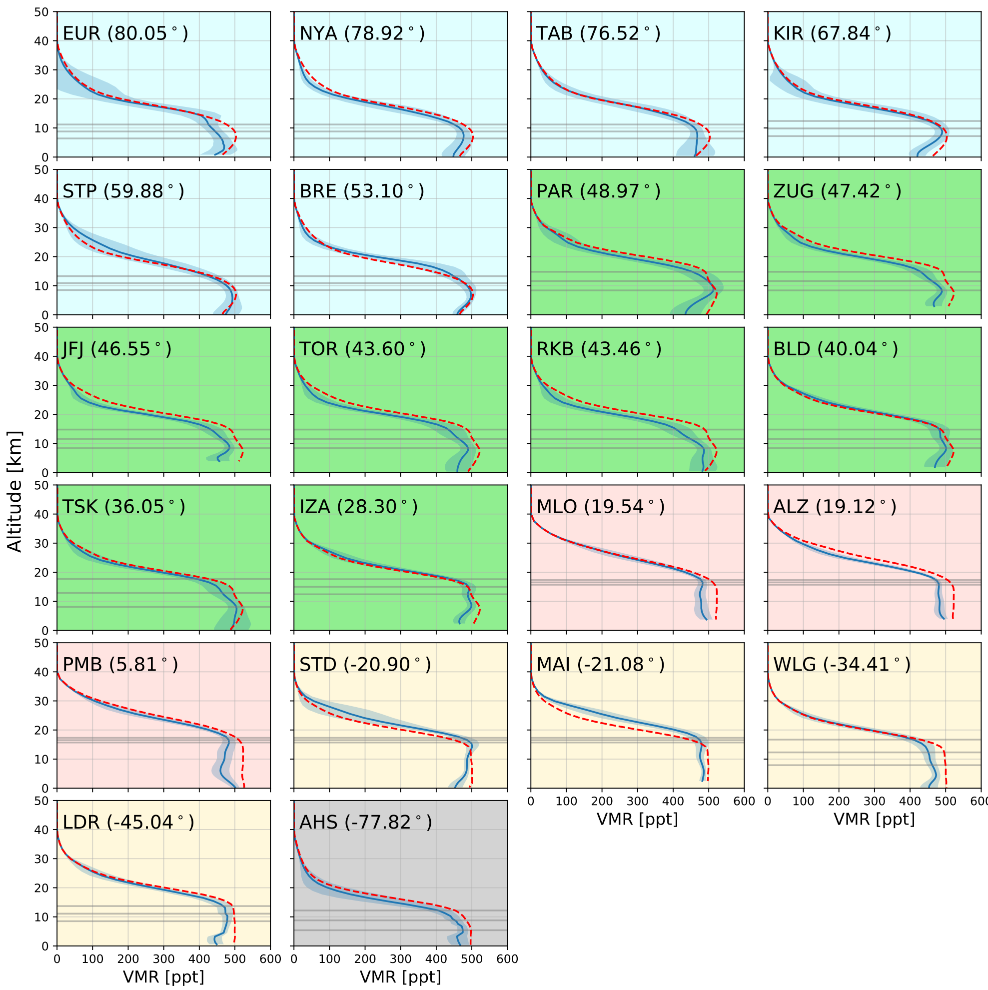

Figure 3. *Mean OCS vertical profiles at all sites (blue continuous lines). The blue shaded area represents the standard deviation of all retrievals. Red dashed lines are the a priori from HIPPO + ACE-FTS data, see Figure 2. The mean tropopause height and 2x standard deviation as defined in the text are shown in horizontal grey lines.*

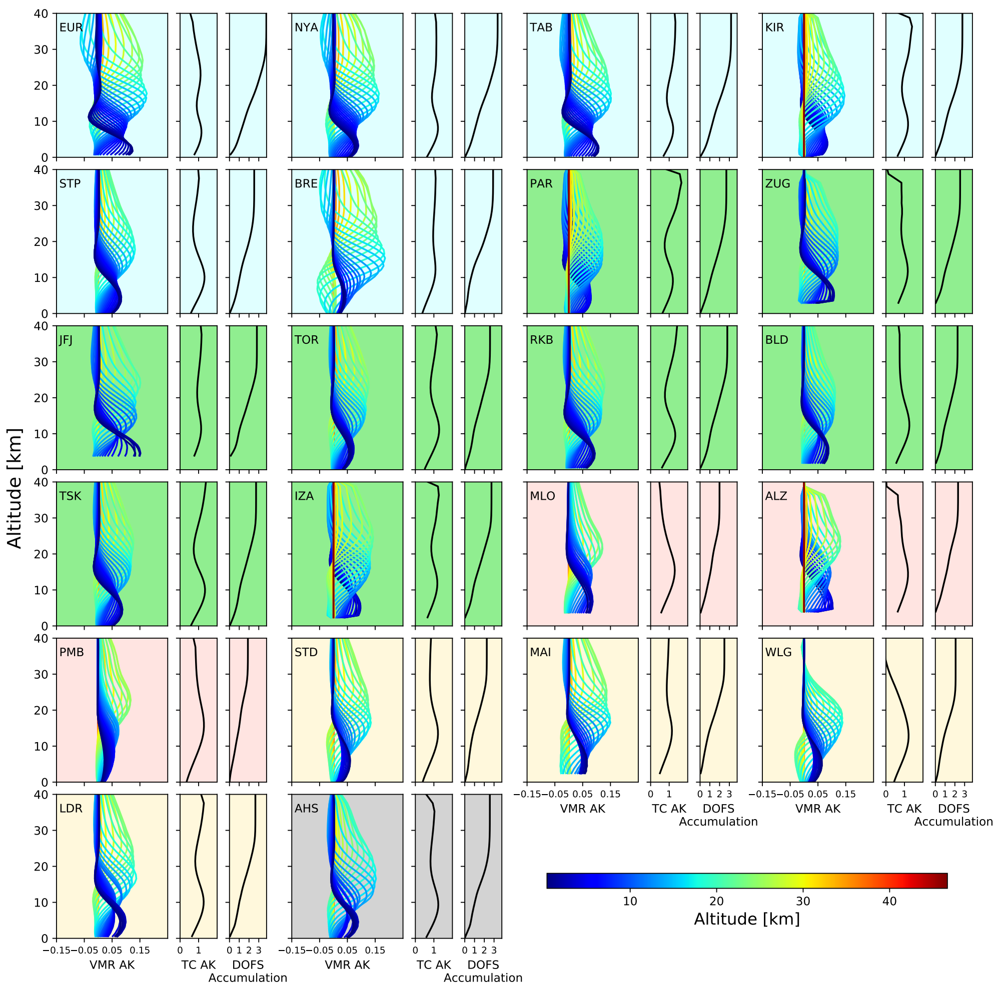

Figure 4. *Characteristics of the retrieval for each station as a function of altitude. The left-most plot per site are the averaging kernels on the retrieval grid color coded by altitude. The center plot is the total column averaging kernel and the rightmost plot is the DOFS, accumulated from the observation altitude to top of atmosphere.*

Table 4. *Typical random, systematic and total uncertainties for a single retrieval by altitude layer for three latitudinally dispersed stations: Thule, Gr, Boulder, Co, USA and Mauna Loa, HI, USA. Values are in pptv for the layers and percent of the mean for the total column. They are average ±1σ for all retrievals for 2019. The right column is the mean DOFS for the same dataset.*

Station	Altitude Region	Random	Systematic	Total	Mean DOFS
TAB	Low Troposphere	11.48 ± 1.27	17.36 ± 3.44	20.99 ± 2.81	0.7
	Free Troposphere	8.21 ± 2.15	20.97 ± 3.69	22.66 ± 4.01	0.6
	Stratosphere	9.72 ± 0.91	28.72 ± 2.09	30.79 ± 2.00	1.9
	Total Column [%]	1.28 ± 0.42	2.77 ± 0.32	3.08 ± 0.35	3.3
BLD	Low Troposphere	12.46 ± 1.48	14.86 ± 2.52	19.56 ± 1.50	0.4
	Free Troposphere	7.03 ± 0.83	16.24 ± 1.03	17.98 ± 0.83	0.8
	Stratosphere	9.27 ± 0.56	31.79 ± 1.66	33.50 ± 1.65	1.4
	Total Column [%]	1.08 ± 0.21	2.84 ± 0.28	3.04 ± 0.33	2.7
MLO	Free Troposphere	6.84 ± 0.89	15.68 ± 1.55	17.40 ± 1.63	1.0
	Stratosphere	6.95 ± 0.51	26.13 ± 1.57	27.14 ± 1.48	0.9
	Total Column [%]	1.02 ± 0.22	2.90 ± 0.18	3.09 ± 0.16	2.0

Table 5. *Bias in percent of the a priori, of the mean retrieved profile for all retrievals at each site, these are the profiles shown in Figure 2*

Station	Low Troposphere	Free Troposphere
EUR	-3.61	-8.16
NYA	-4.66	-5.21
TAB	-2.98	-6.73
KIR	-10.02	-4.33
STP	1.21	-2.08
BRE	-1.53	-1.05
PAR	-11.92	-4.06
ZUG	-8.32	-7.39
JFJ	-	-8.89
TOR	-7.49	-6.96
RKB	-3.25	-7.23
BLD	-5.28	-6.87
TSK	-0.80	-3.75
IZA	-8.41	-4.27
MLO	-	-8.02
ALZ	-	-7.50
PMB	-7.29	-10.21
STD	-7.17	-1.41
MAI	-2.90	-3.04
WLG	-8.06	-7.32
LDR	-10.57	-4.92
AHS	-6.83	-5.12

Table 6. *Tropopause height statistics determined from NCEP data for all observation days at all sites binned in ˜10° zonal regions excluding subtropic and southern mid-latitudes.*

Station	Latitude [$^{\circ}N$]	Mean ± SD [km]	Max. [km]	Min. [km]	Pk-Pk [km]	Latitude Bin
EUR	80.1	8.8 ± 1.1	11.2	6.2	2.0	90-70°N 8.8±1.2 Pk-Pk=2.1
NYA	78.9	8.9 ± 0.9	11.3	6.7	2.2	
TAB	76.5	8.7 ± 1.1	11.4	5.7	2.2	
KIR	67.8	9.8 ± 1.1	12.9	6.8	1.4	70-60°N
STP	59.9	10.5 ± 1.0	12.8	7.2	1.9	60-50°N 10.9±1.2
BRE	53.1	11.2 ± 0.9	14.0	8.2	1.5	Pk-Pk=1.7
PAR	49.0	11.7 ± 0.9	13.6	9.1	1.4	
ZUG	47.4	11.7 ± 1.1	15.1	8.3	2.0	
JFJ	46.5	11.7 ± 1.1	15.7	8.1	2.0	50-40°N 11.6±1.4
TOR	43.6	12.0 ± 1.8	15.8	7.6	4.2	Pk-Pk=3.0
RKB	43.5	10.7 ± 2.0	16.5	7.4	5.4	
BLD	40.0	13.3 ± 1.8	16.4	9.5	4.3	
TSK	36.0	12.6 ± 2.4	16.7	7.3	6.6	40-30°N
IAZ	28.3	15.1 ± 1.1	17.6	11.2	2.1	30-20°N
MLO	19.5	16.1 ± 0.6	17.6	11.9	0.8	
ALZ	19.1	16.5 ± 0.4	17.6	15.7	1.0	20°N-25°S 16.5±0.4
PMB	5.8	16.5 ± 0.2	17.2	16.0	0.5	Pk-Pk=0.7
STD-MAI	-20.9	16.6 ± 0.3	17.4	15.8	0.5	
WLG	-34.4	12.3 ± 2.0	17.4	8.2	4.4	25-45°S 11.7±1.6
LDR	-45.0	11.1 ± 1.2	16.6	8.6	2.3	Pk-Pk=3.3
AHS	-77.8	8.8 ± 1.5	14.1	6.2	3.8	50-90°S

Table 7. *Proxy, description and sources of proxy data for FT SMR-COC regression analysis.*

ID	Name	Description	Source
QBO	Quasi-biennial oscillation	Based on equatorial stratosphere winds at 30 and 10 hpa	http://www.geo.fuberlin.de/en/met/ag/strat/produkte/qbo/index.html
AO	Arctic oscillation	Monthly values from NCEP	http://www.cpc.ncep.noaa.gov/products/precip/CWlink/daily_ao_index/ao.shtml
ENSO	El Niño/Southern Oscillation index	Multivariate El Niño/Southern Oscillation index (MEI)	http://www.esrl.noaa.gov/psd/enso/mei/
NDVI	Normalized Difference Vegetation Index	MODIS/Terra Vegetation Indices, Monthly L3 Global 0.05 Deg (MOD13C2) Version 6.	https://lpdaac.usgs.gov/products/mod13c2v006/
CHLOR	Chlorophyll index	Monthly values from MODIS/Aqua at 4km resolution	https://oceancolor.gsfc.nasa.gov/
SST	Sea Surface Temperature	Monthly values from MODIS/Aqua using the 1μ m and 12μ m bands at 4km	https://oceancolor.gsfc.nasa.gov/
SIC	Sea ice Concentration	National Climatic Data Center Monthly mean analyses	https://rda.ucar.edu/datasets/ds277.0/index.html#!description

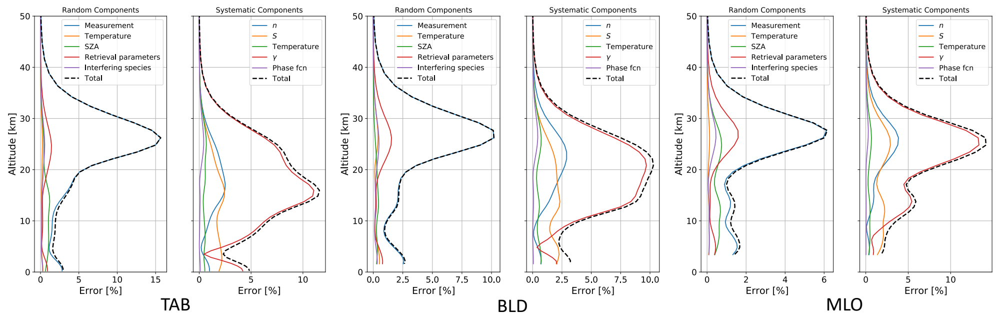

Figure 5. *Uncertainty profiles for three latitudinally dispersed stations: Thule, Gr, Boulder, Co, USA and Mauna Loa, HI, USA (left, center, right respectively). For each site, the left panel are random components and total and the right panel are systematic components and total. These profiles for a single retrieval of approximately 2 minutes measurement integration time and are given in percent of the a priori profile. Components are described in the text but in particular systematic components: γ is the Lorentzian air broadening half width, n is the exponent of the dependence of the air broadening halfwidth and S is the line intensity.*

Table 8. *Calculations of the stratospheric lifetimes of OCS using Eqn. 4 and measured FT OCS and N_2O concentrations across the five latitude bands.*

Latitude Band [° N]	A [ppb/ppb]	Mean FT OCS [ppb]	Mean FT N_2O [ppb]	R^2	Average Lifetime [year]
90. - 50.	482.9 ± 6.8	0.472 ± 0.028	315.8 ± 10.8	0.79	84.5 ± 15.6
50. - 20.	327.3 ± 4.6	0.483 ± 0.020	318.4 ± 5.3	0.86	58.0 ± 10.3
20. - -20.	309.3 ± 13.4	0.477 ± 0.016	319.4 ± 4.5	0.83	54.1 ± 9.7
-20. - -50.	448.1 ± 10.2	0.468 ± 0.012	314.3 ± 6.7	0.90	78.1 ± 13.7
-50. : -90.	577.6 ± 20.9	0.475 ± 0.008	310.2 ± 6.2	0.89	103.4 ± 18.3

Figure 6. *Time series of OCS Total Column for all sites on the same ordinate and abscissa scale. Gray circles represent the monthly mean observational data. The blue line is the seasonal modulation and trend component of the monthly mean total column using Eqn. 1).*

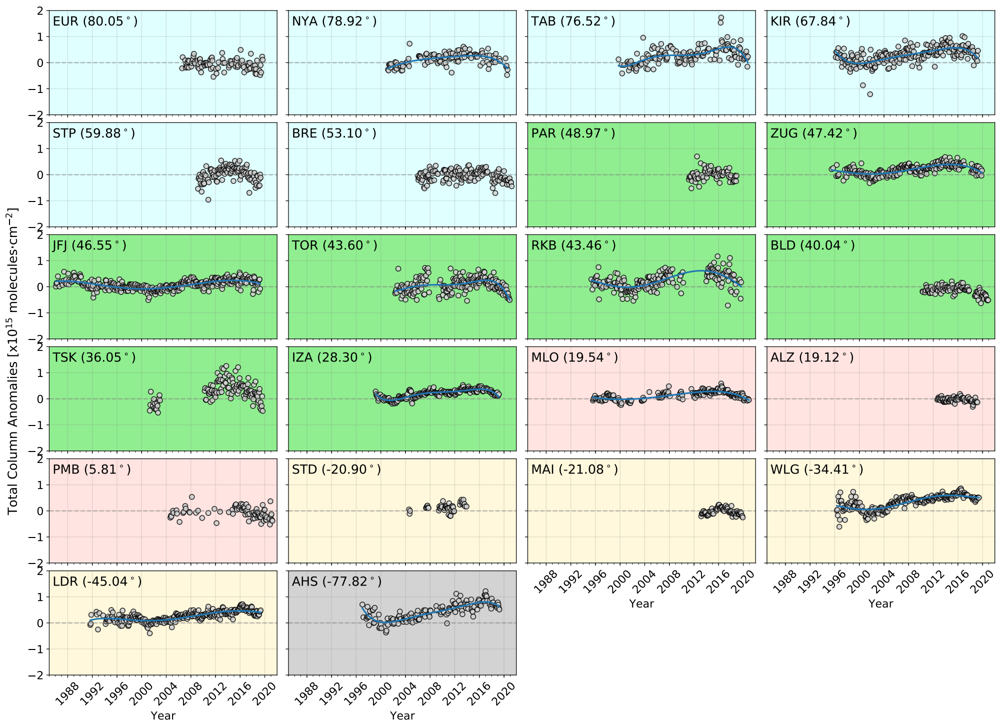

Figure 7. *Time series of OCS Total Column anomalies for all sites on the same ordinate and abscissa scale, see text for derivation. Gray circles represent monthly mean observational anomalies. The blue curve is fit to the anomaly with a 5^{th} order polynomial showing changes in trend to several of the longest time series (NYA, TAB, KIR, ZUG, JFK, TOR, RKB, IZA, MLO, WLG, LDR and AHS). (see Eqn. 1).*

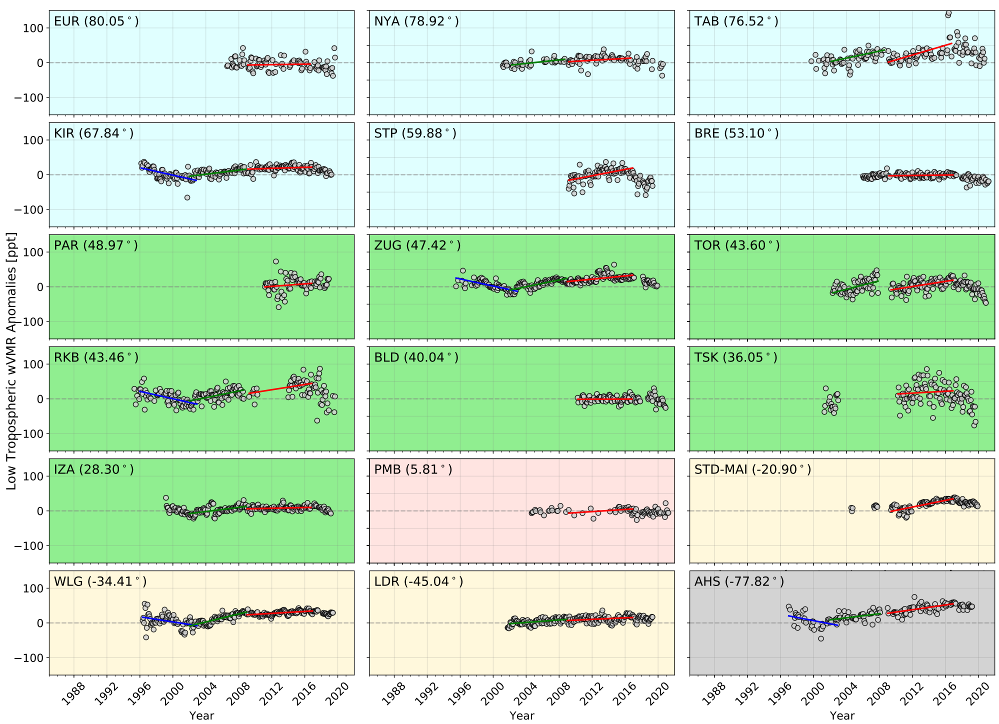

Figure 8. *Time series of weighted OCS anomalies (wVMR) for the lower troposphere for all sites. Gray circles represent monthly mean anomaly. The blue line is the linear trend for period 1, green is for period 2 and red is for the most recent time period. See Eqn. 1 and text for definition of anomaly series.*

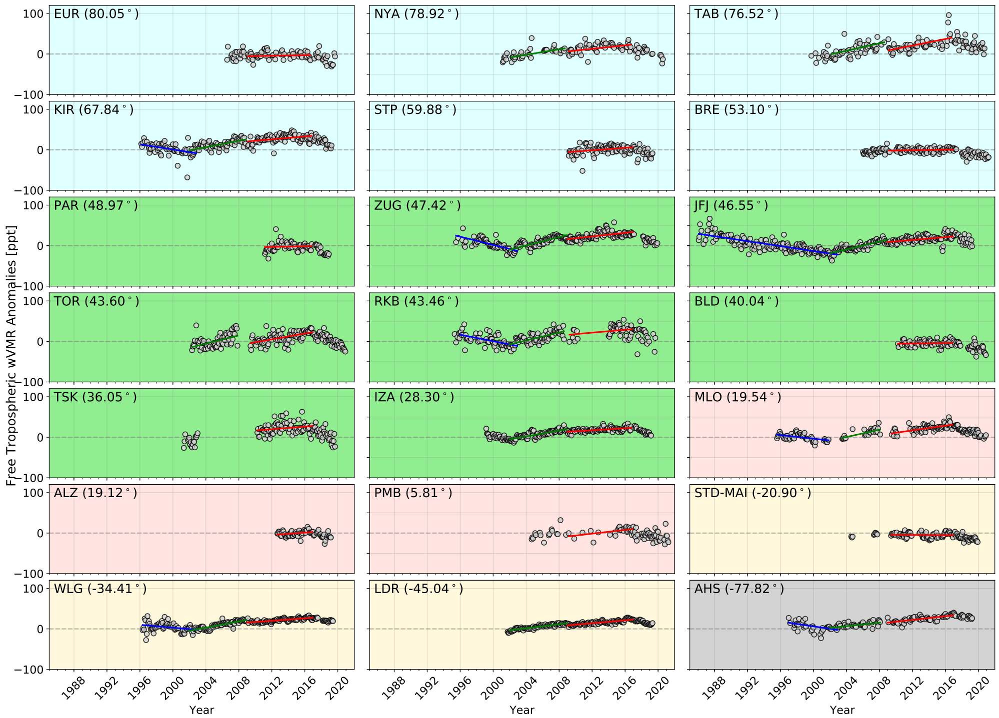

Figure 9. *Time series of weighted OCS wVMR anomalies in the free troposphere for all sites. Annotated similarly as Figure 8.*

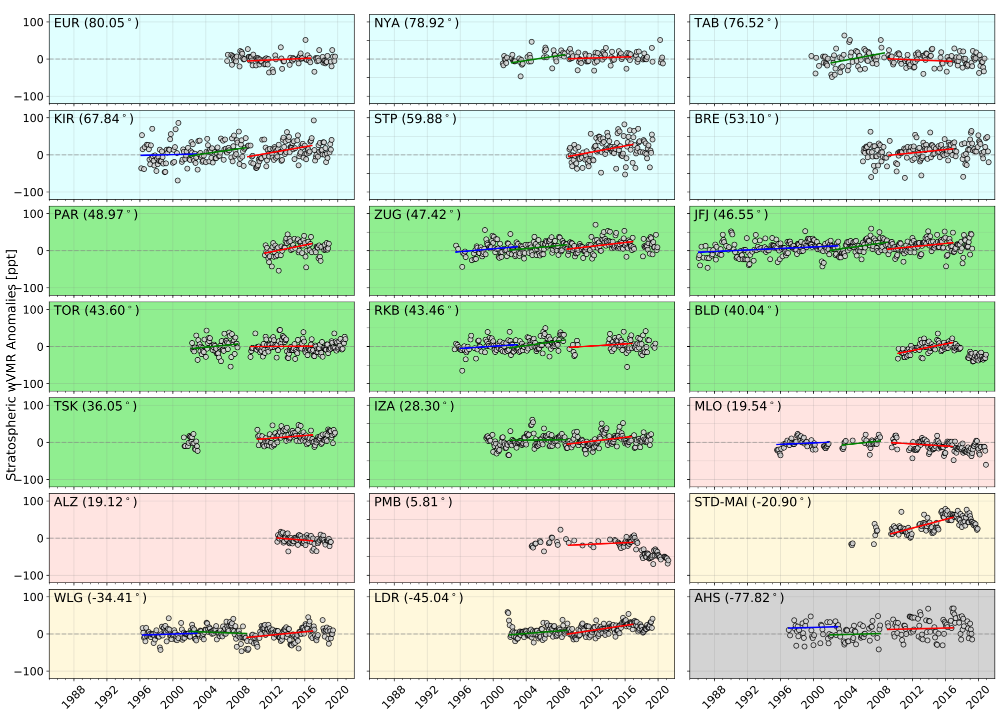

Figure 10. *Time series of weighted OCS wVMR anomalies for the stratosphere component for all sites. Annotated similarly as Figure 8.*

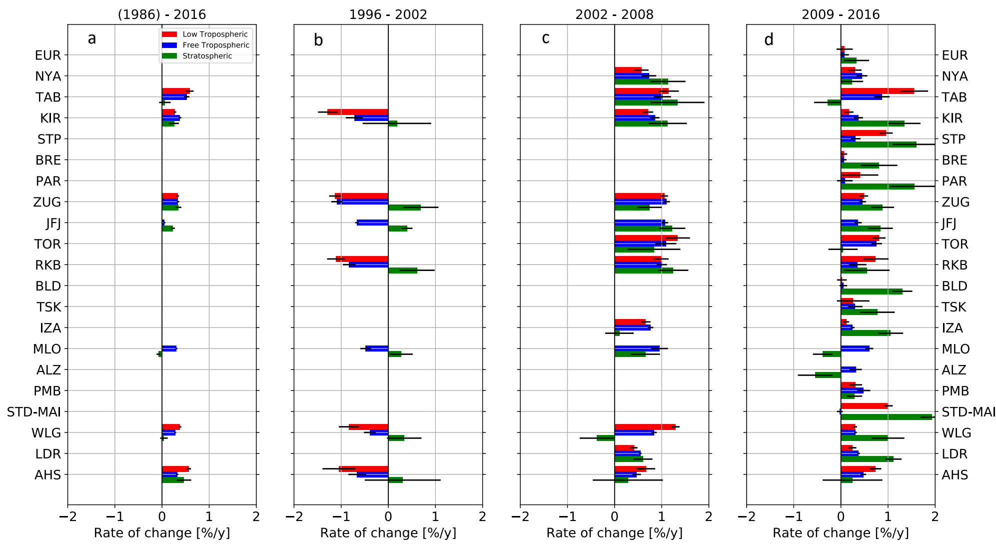

Figure 11. *Trends by time period for all stations and for all three altitude ranges, listed by high to low latitude. Red represents the lower troposphere, blue the free troposphere and green the stratosphere. The left panel (a) are trends for only those sites with data from 1996, then increasing time period left to right, b: 1996-2002, c: 2002-2008, and d: 2009-2016 and so including more recently begun stations. Note: the TAB dataset in the 1996-2016 panel begins in 1999, PAR dataset in panel 2009-2016 begins in 2011, ALZ dataset in panel 2009-2016 begins in 2012.*

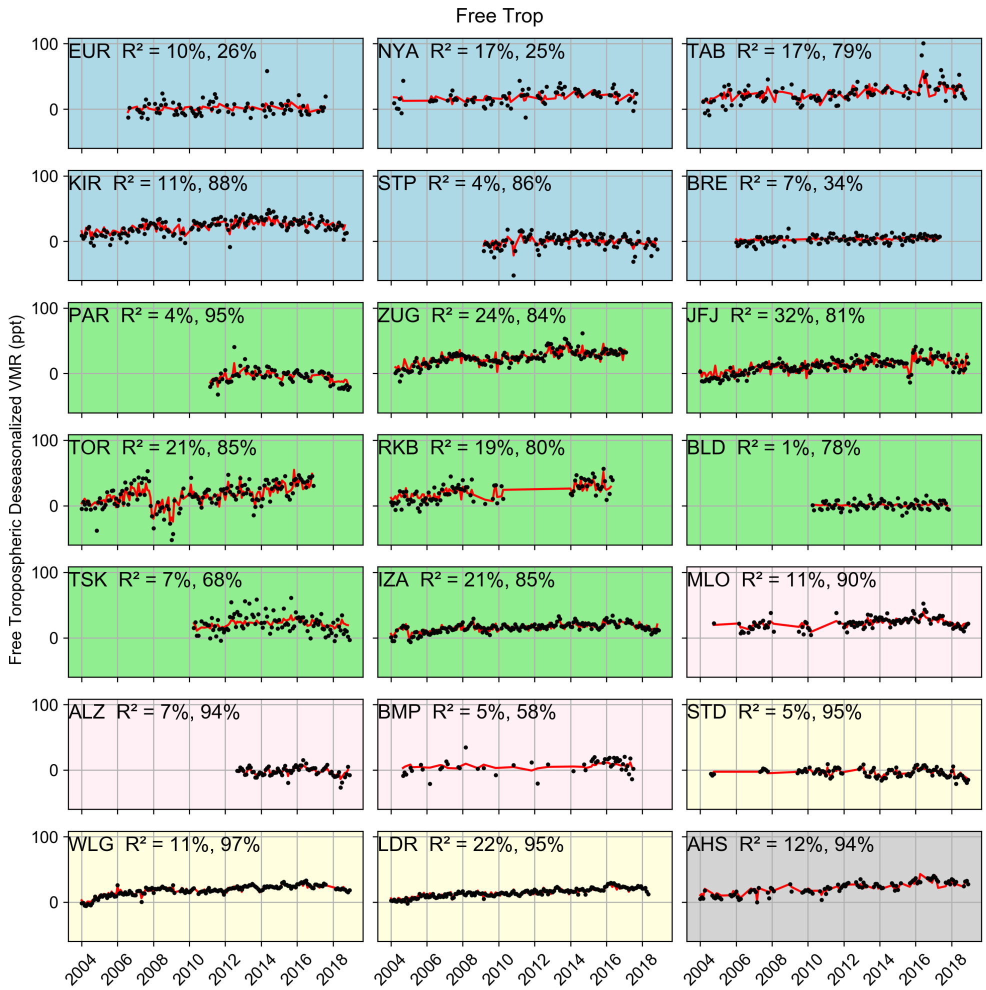

Figure 12. *Final fit of dominant meridional and zonal proxies to free tropospheric anomalies using the Cochrane-Orcutt auto-regression analysis.* R^2 *with and without auto-regression are shown in upper left of the plot for each station.*

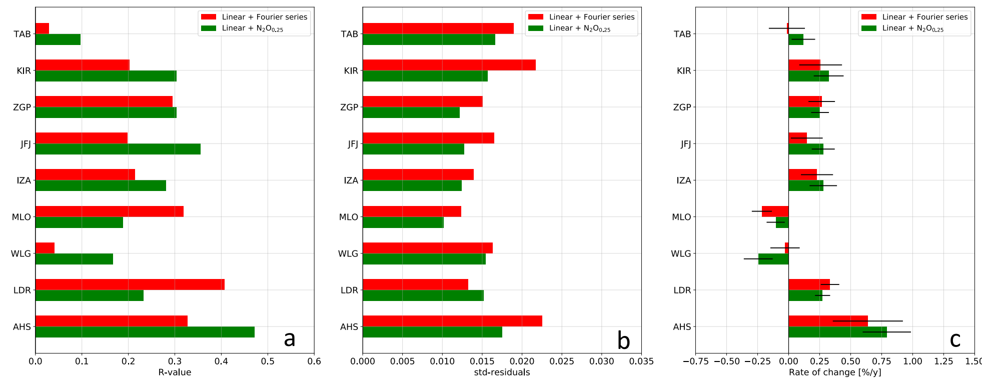

Figure 13. *Results of the N_2O proxy analysis on the longest stratospheric data records from 2001 − 2016. Panel a are R-values of the regression and show generally higher correlations except for MLO and LDR. Panel b is a comparison of fit residuals showing slightly improved regressions using the N_2O proxy. And Panel c compares the linear trends. Using the N_2O proxy most trends are slightly increased except WLG and LDR but all within uncertainties.*

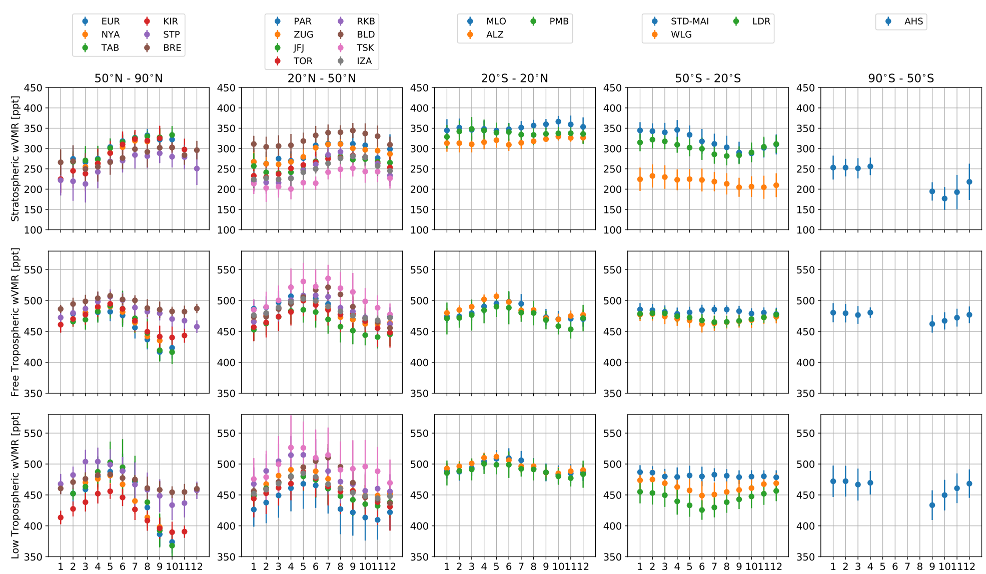

Figure 14. *Annual cycle using monthly mean wVMR for all stations. Panels left to right are decreasing latitude bins (see Table 3) and increasing altitude bins bottom to top. All data are used irrespective of station time series duration.*

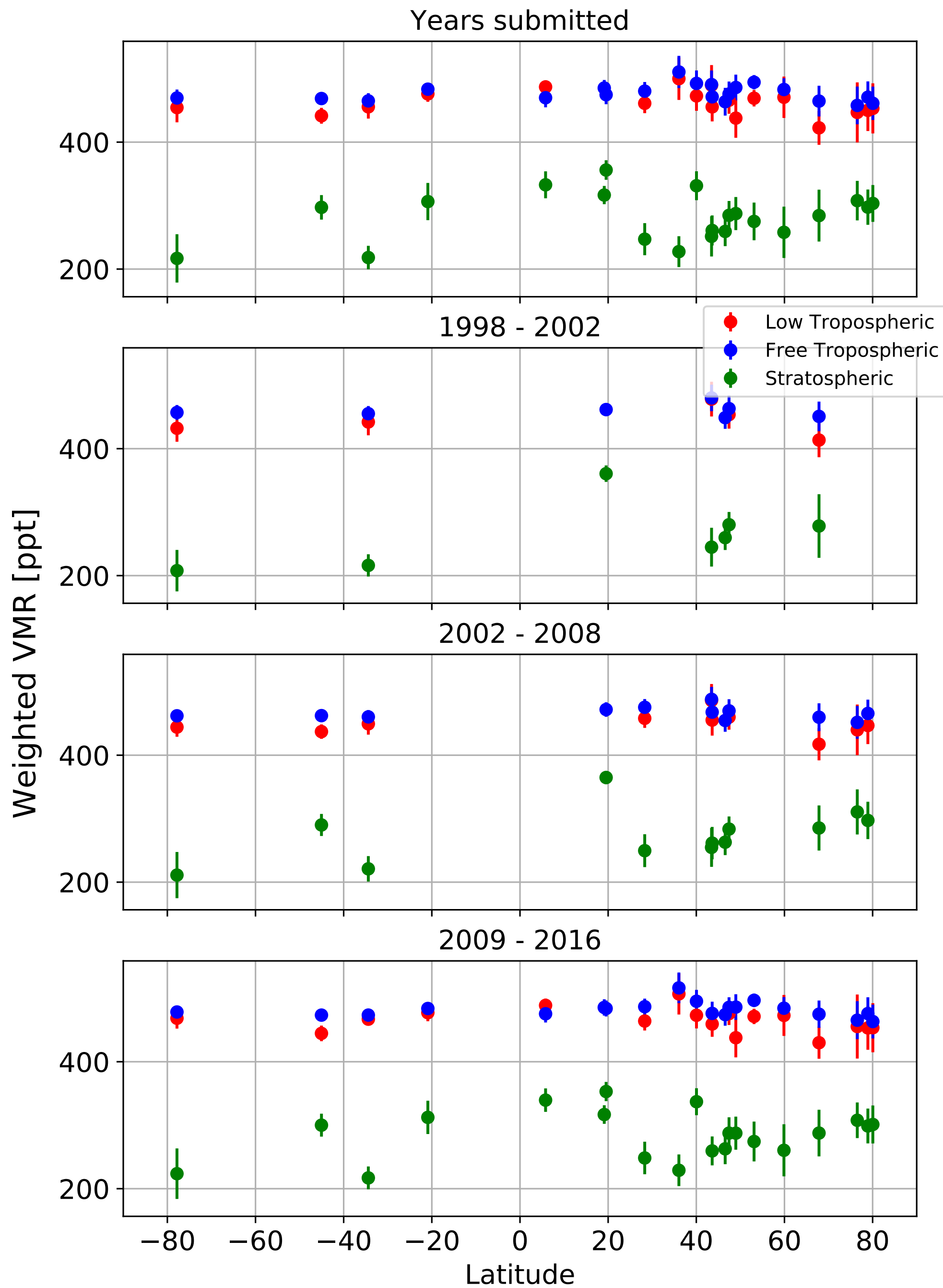

Figure 15. *All wVMR data versus latitude and panels represent estimated monotonic trend periods. Color codes are green: stratosphere, blue, free troposphere and red is the lower troposphere.*